Design, Theoretical and Experimental Investigation of Tensile-strained Germanium Quantum-well Laser Structure

Mantu K. Hudait^{†*}, Felipe Murphy-Armando^{‡,} Dzianis Saladukha[§], Michael B. Clavel[†],
Patrick S. Goley[†], Deepam Maurya[⊥], Shuvodip Bhattacharya[†], and Tomasz J. Ochalski [§]

[†]Advanced Devices & Sustainable Energy Laboratory (ADSEL), Bradley Department of
Electrical and Computer Engineering, Virginia Tech, Blacksburg, Virginia 24061

[‡]Tyndall National Institute, Lee Maltings, Cork T12 R5CP, Republic of Ireland

[§]The Centre for Advanced Photonics & Process Analysis, Munster Technological University
at Tyndall National Institute, Cork T12R5CP, Republic of Ireland

[⊥]Center for Energy Harvesting Materials and Systems (CEHMS), Mechanical Engineering,
Virginia Tech, VA 24061, USA

ABSTRACT: Strain and bandgap engineered epitaxial germanium (ε-Ge) quantum-well (QW) laser structures were investigated on GaAs substrates theoretically and experimentally for the first time. In this design, we exploit the ability of InGaAs layer to simultaneously provide tensile strain in Ge (0.7% to 1.96%) and sufficient optical and carrier confinement. The direct band-to-band gain, threshold current density (J_{th}) and loss mechanisms that dominate in the ε-Ge QW laser structure, were calculated using first-principles-based 30-band k.p electronic structure theory, at injected carrier concentrations from $3x10^{18}$ cm⁻³ to $9x10^{19}$ cm⁻³. The higher strain in ε-Ge QW increases the gain at higher wavelengths; however, a decreasing thickness is required by higher strain due to critical layer thickness for avoiding strain relaxation. In addition, we predict that a J_{th} of 300 A/cm² can be reduced to <10 A/cm² by increasing strain from 0.2% to 1.96% in ε-Ge lasing media. The measured room temperature photoluminescence spectroscopy demonstrated direct bandgap optical emission from the conduction band at Γ-valley to heavy-hole (0.6609 eV) from 1.6% tensile strained Ge/In_{0.24}Ga_{0.76}As heterostructure grown by molecular beam epitaxy, is in agreement with the value calculated using 30-band k.p

theory. The detailed plan-view transmission electron microscopic (TEM) analysis of 0.7% and

1.2% tensile strained ε-Ge/InGaAs structures, exhibited well-controlled dislocations within

each ϵ -Ge layer. The measured dislocation density is below $4x10^6$ cm⁻² for 1.2% ϵ -Ge layer,

which is an upper bound, suggesting the superior ε-Ge material quality. Structural analysis of

the experimentally realistic 1.95% bi-axially strained $In_{0.28}Ga_{0.72}As/13$ nm ϵ -Ge/ $In_{0.28}Ga_{0.72}As$

QW structure demonstrated strained Ge/In_{0.28}Ga_{0.72}As heterointerface with minimal relaxation

using x-ray and cross-sectional TEM analysis. Therefore, our monolithic integration of strained

Ge QW laser structure on GaAs and ultimately transfer the process to Si substrate via

InGa(Al)As/III-V buffer architecture, would provide a significant step towards photonic

technology based on strained Ge on Si platform.

KEYWORDS: germanium, epitaxy, molecular beam epitaxy, heterostructure, laser

2

INTRODUCTION

Integration of group-IV (e.g., Ge, SiGe, GeSn) based light sources on silicon (Si) substrate have been intensively studied for decades without technological impact. It was believed this lack of success was due to the quality of materials synthesis and approaches taken to demonstrate the light sources on Si. However, excellent progress has been made in recent years for the development of group-IV based light sources, ¹⁻¹³ and opening up the possibility to have a major impact in the optoelectronic research field. In particular, the development of a novel short-wavelength near-infra-red (NIR) tunable laser sources, in the range of 1.7 μm to 2.5 μm, is important for optical coherence tomography (OCT) and biomedical applications. 14-17 It has recently been discovered with non-coherent light that spectrum in the short-wavelength infrared (SWIR) can achieve much higher resolution and penetration in opaque living tissue than NIR, especially in brain tissue imaging. 14-17 In OCT, another property affecting the resolution is the emission bandwidth: the wider the bandwidth the higher the resolution achievable. However, there are a lack of sources in the SWIR that have the combination desired intensity and bandwidth to further enhance OCT in this spectral range. In addition, in the current Si microprocessors, copper interconnect bottlenecks due to resistive power loss for both interchip and intra-chip communication, are calling for integrated light sources. A desirable alternative would be an on-chip integrated photonic devices with Si CMOS technology. However, indirect band gap semiconductors, Si and Ge, are usually unsuitable for laser diodes due to their inefficient radiative recombination. In the work reported in Ref [18], single 1,183nm continuous-wave off-chip solid-state laser acts as the light source for the demonstration of an electronic-photonic microprocessor chip that enables VLSI technology, by adding nanophotonics as a new design dimension. It has also been proposed that photonic devices to be integrated directly with electronics in CMOS process, enabled a fully functioning electronicphotonic system on a single chip, to be produced in a high-volume electronics foundry. To

achieve such aggressive goal, extensive researches were pursuing on GeSn materials as a function of tin (Sn) alloy composition ^{1-13, 19-31} on Si or GeSn bonded with virtual substrate as well as III-V lasers grown on ^{26, 32, 33} or bonded to Si¹⁹ substrate. Liu et al.³⁴ played the thermal mismatch between the deposited Ge layer and the Si substrate that results in a $\sim 0.2\%$ tensile strain in Ge layer during material synthesis combined with *n*-type doping ($\geq 7 \times 10^{19}$ cm⁻³) in order to compensate the pseudo energy difference between the Γ- and L-valley (~130 meV) at conduction band for the emission wavelength of 1.55 µm. This approach resulted in a weak optical gain and emission from the direct gap transition of a deposited Ge layer. Although this research work is promising, the defects and dislocations due to lattice mismatch in the active Ge lasing media on Si in addition to the fixed laser wavelength due to the fixed strain/doping suggest that an alternative approach for a tunable wavelength Ge laser on Si is needed. The modification could be the Ge-based quantum-well (QW) configuration with proper barrier layers such that they will provide both carrier confinement (through valence and conduction band offsets) and optical confinement (through differences in refractive indices), and hence for achieving low threshold current density (J_{th}) and high efficiency (η) . This hybrid integration of strained Ge (ε-Ge) QW design through barrier materials-based electronic-optoelectronic devices with Si CMOS technology would revolutionize technology needs in the near future.

In this paper, we have designed and demonstrated a 1.95% strained Ge QW laser structure (In_{0.28}Ga_{0.72}As/13nm ε-Ge/In_{0.28}Ga_{0.72}As) through modeling and experimentally *via* strain and bandgap engineered epitaxial Ge layer using interconnected dual chamber solid source molecular beam epitaxy (MBE) deposition system. This method offers design flexibility to provide tunable strain to Ge and hence the bandgap, by changing indium (In) composition in the In_xGa_{1-x}As barrier materials during material synthesis. In addition, this approach provided direct bandgap Ge and type-I band alignment,³⁵ both being needed for carrier and optical confinement. These Ge QW laser structures were characterized using high-resolution x-ray

diffraction for strain analysis and structural properties, cross-sectional and plan-view transmission electron microscopy (TEM) for defect properties. The room temperature optical properties using photoluminescence (PL) spectroscopy, materials analysis, and Ge laser modeling using FIMMWAVE ³⁶ were demonstrated as a first step towards the development of Ge-based light sources. Therefore, our monolithic heterogeneous integration of tunable wavelength Ge laser structure (*via* strain and bandgap engineering) on GaAs and ultimately transfer the process to Si substrate using InGa(Al)As/III-V buffer architecture, ^{31, 37-41} would provide a paradigm shift for photonic technology on Si.

RESULTS AND DISCUSSION

Strain dependent ε -Ge/ln_xGa_{1-x}As electronic structure calculations: The first step in demonstrating that strained ε -Ge can produce an enhancement in optical gain is determining the strain and layer thickness conditions that increase direct band electron-hole recombination. Figure 1 shows the calculated electronic band structure of Ge with applied (100) biaxial strain corresponding to Ge grown on $In_xGa_{1-x}As$ at different In concentrations, and that correspond to those grown and studied in this work. In terms of band structure, optical gain depends on the competition between the single Γ and the four L conduction band valleys in Ge. In unstrained bulk Ge, the minimum of the conduction band is at the four L-valleys, while the direct Γ -valley lies 120 meV above the L-valley minimum (see Fig. 1a). Biaxial tensile strain lowers the Γ -valley, reaching the indirect-to-direct conduction band transition at In content x = 0.24, corresponding to a strain of $\varepsilon = 1.62\%$, and is consistent with previous observations.^{31, 40} Further strain turns Ge into a direct band semiconductor. The separation between the L-valley and Γ -valley with increasing strain, as indicated by green and pink lines (by increasing indium content in the $In_xGa_{1-x}As$ layer) in each case, shown in the inset of Figure 1. It is important to note that the density of states (DOS) of the L-valley is ~50 times larger than that of the Γ -

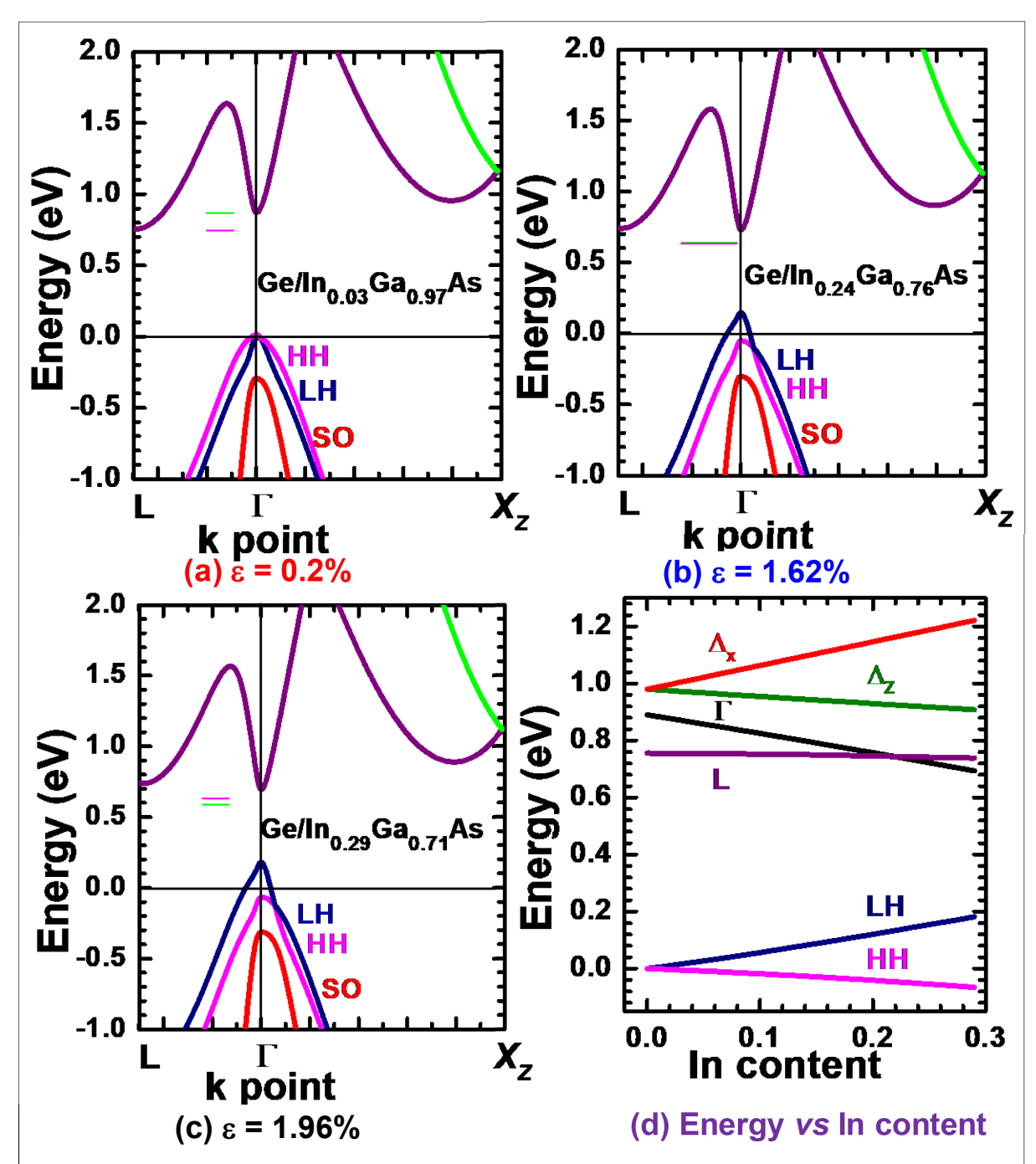


Figure 1: Electronic band structure of strained Ge calculated using a 30-band **k.p** approach at 0K. Biaxial strain applied is (a) 0.2%, (b) 1.62% and (c) 1.96%. Xz is the X point in the direction of growth. The inset shows the energy difference of the conduction band minimum on the left (L) and the gamma point (Γ) in each strain amount. At 1.96% strain level, the Γ point is lower than the L point in the conduction band. (d) Theoretical bandgap versus indium (In) dependence of Ge/In_xGa_{1-x}As system and the indirect to direct band gap of Ge occurs at about 22-24% In composition in In_xGa_{1-x}As.

relative to the Γ -valley in the energy dispersion shown in **Fig. 1a**). Therefore, most of the injected electrons will populate the L-valley unless strain can induce enough separation between the valleys. Lowering the Γ -valley sufficiently below the L-valley (see **Figure 1c**) so that most injected electrons populate the Γ -valley should see a very large increase in gain. However, gain will increase at longer wavelengths and lower injection densities than in bulk Ge with any lowering of the conduction band Γ -valley, as this is the only direct-band recombination channel. The high strains required to sufficiently lower the Γ -valley to capture most injected carriers may limit the thickness of the ε -Ge that can be grown, due to critical thickness constraints. As we will see later, quantum confinement pushed the Γ -valley (see **Figure 1d**) higher in energy faster than the L-valley, due to the small effective mass of the Γ -valley. Therefore, the thickness at which the Ge active layer can be grown will play a crucial role in the gain achievable in group-IV based QW laser.

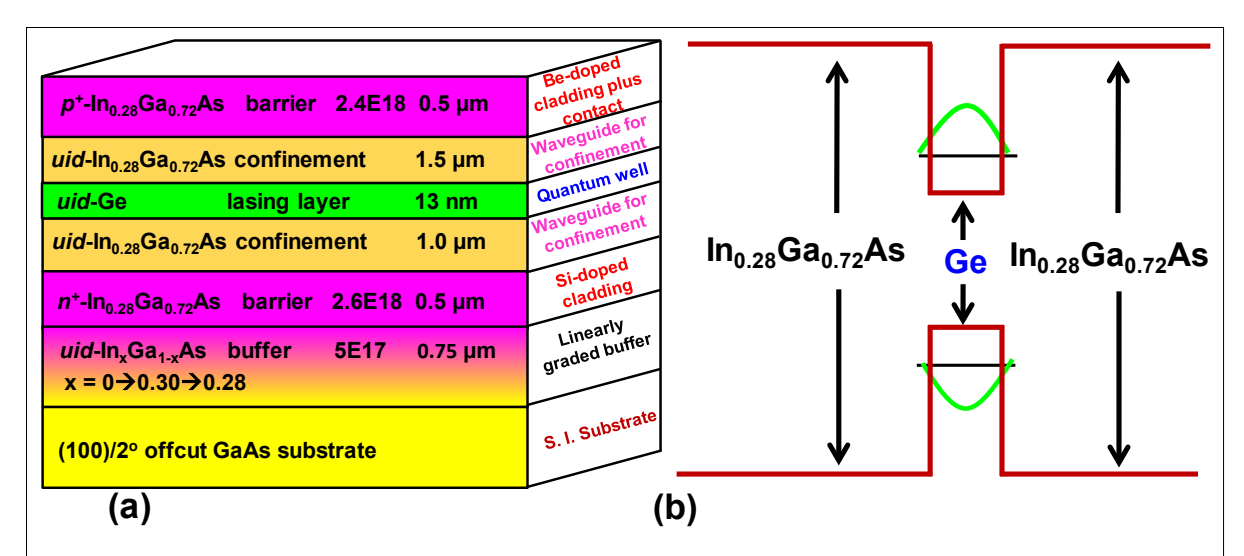


Figure 2: (a) Ge laser structure on GaAs with tunable surface lattice constant of mixed-cation InGaAs ternary buffer layer architecture. The III-V optical cavity is also designed for the tunable wavelength Ge laser structure, and (b) the schematic representation of energy band diagram for the In_{0.28}Ga_{0.72}As/ ε -Ge/In_{0.28}Ga_{0.72}As laser structure (it is not to scale).

ε-Ge quantum-well laser design and modeling: - selection of thickness, strain, and doping density: Figure 2 shows the bandgap and 1.95% tensile-strain engineered Ge QW laser

structure on GaAs substrate as well as a schematic representative energy band diagram using In_xGa_{1-x}As strain template along with In_{0.28}Ga_{0.72}As carrier and optical confinement layer. This Ge QW laser structure was modeled using FIMMWAVE mode solver from Photon Design.³⁶ This FIMMWAVE provides full vectorial mode solver suitable for modeling waveguide and the grating structures with different geometries. In the Ge laser structure, the In composition in linearly graded In_xGa_{1-x}As buffer can be varied to a targeted In composition for achieving different tensile strained amount in Ge. This in turn changes the strain induced bandgap of Ge and hence the lasing wavelength. One can replace the InGaAs cladding/waveguide layer by InAlAs/AlGaInAs layer in the Ge QW laser structure for superior optical and carrier confinement due to its larger band offsets and differences in refractive indexes. In our design, we exploit the ability of Ge/III-V heterostructures to induce epitaxial stress in the Ge thin-film and simultaneously provide sufficient optical and carrier confinement so as to realize a practical lasing structure. A first-principles computation of the Ge/InAlAs electronic structure reveals band offsets $\geq 0.56 \pm 0.1$ eV at the ε -Ge/In_xAl_{1-x}As heterointerface, ⁴² corroborated with our experimental band offset results. Utilizing a MBE growth process, discussed below, we have demonstrated the feasibility of integrating the tensile-strained In_xGa_{1-x}As/ε-Ge/In_xGa_{1-x}As QW laser structure on GaAs substrate. The 13 nm ε-Ge layer was embedded within lower refractive index layers of InGaAs for confining the optical mode and maximizing mode intensity at the intrinsic region of the heterostructure. In the center of the optical waveguide, the ε-Ge QW will provide a confinement for electrons and holes. One of the most critical design parameters for the Ge laser structure are the optical cavity and the active material. The specific thickness of the optical waveguide and finally the laser source geometry can be designed and optimized by employing Eigen mode solution methods build in FIMMWAVE. 36

Figure 3 shows the simulated energy density profiles and transverse electric (TE) mode of 1.95% strained ε -Ge QW structure. Laser mode is confined in the InGaAs layers above and

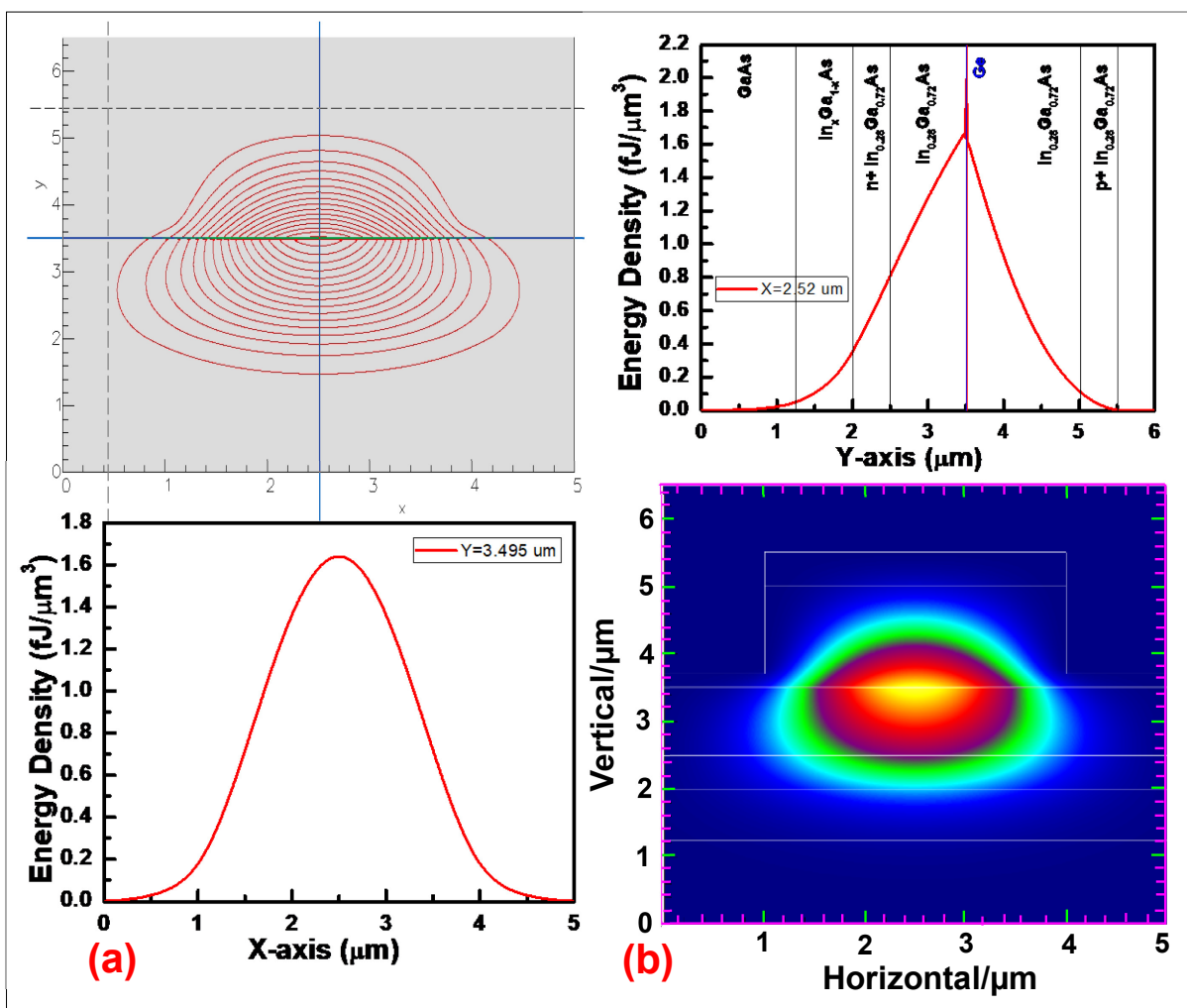


Figure 3: Simulated (a) energy density profiles, and (b) TE mode of the 1.95% ε -Ge laser structure using FIMMWAVE.

below active ε -Ge lasing medium, shown in Figure 3a and 3b. Vertical and horizontal energy density profiles visualize intensity drop to the edges of the InGaAs layers. According to vertical cross-section in the center of mode, $\sim 84\%$ of TE mode is confined in the undoped In_{0.28}Ga_{0.72}As region. In addition, the mode penetration is higher into the bottom InGaAs layer, and it was due to the abrupt refractive index change from the top InGaAs layer to air at upper than the bottom barrier layer. However, the majority of the TE mode can be confined within the ε -Ge layer (its depend on the layer thickness and amount of strain) by inserting a large bandgap Al_{0.3}In_{0.28}Ga_{0.72}As (lower refractive index) layer on both sides of the In_{0.28}Ga_{0.72}As/ ε -Ge/In_{0.28}Ga_{0.72}As lasing media, as shown in **Figure 4**. The refractive index of each layer is also included for better understanding of the optical confinement. In this structure, the total

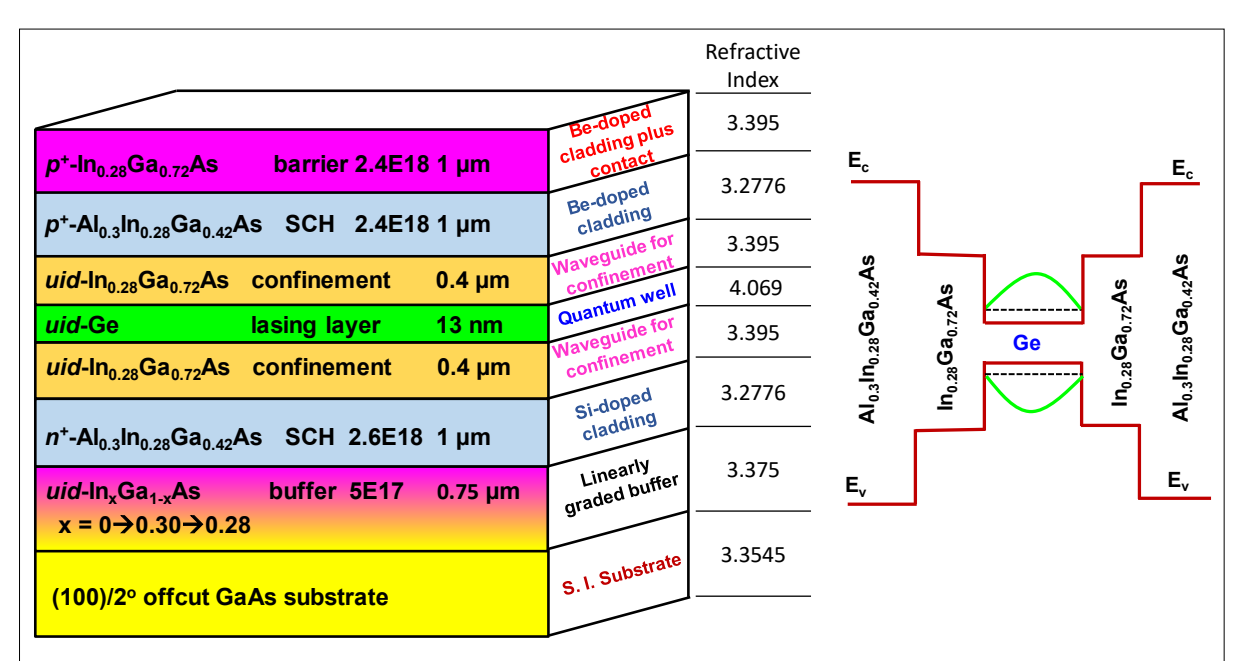


Figure 4: 1.95% strained Ge laser structure on GaAs substrate with InGaAs ternary buffer. The AlInGaAs layer on both side of ε -Ge lasing media is for superior optical and carrier confinement, which is acting as separate confinement heterostructure. The large difference in refractive index between Ge lasing media and adjacent AlInGaAs barrier layer is to provide an optical confinement. The schematic energy band diagram for the ε -Ge laser structure is shown in right (it is not to scale).

 $In_{0.28}Ga_{0.72}As$ layer thickness in each side of εdivided Ge is into combination of $In_{0.28}Ga_{0.72}As$ and $Al_{0.3}In_{0.28}Ga_{0.42}As$ layers. Here, the Al_{0.3}In_{0.28}Ga_{0.42}As layer act as a separate confinement heterostructure (SCH) and the large differences in refractive indices between the ε-Ge

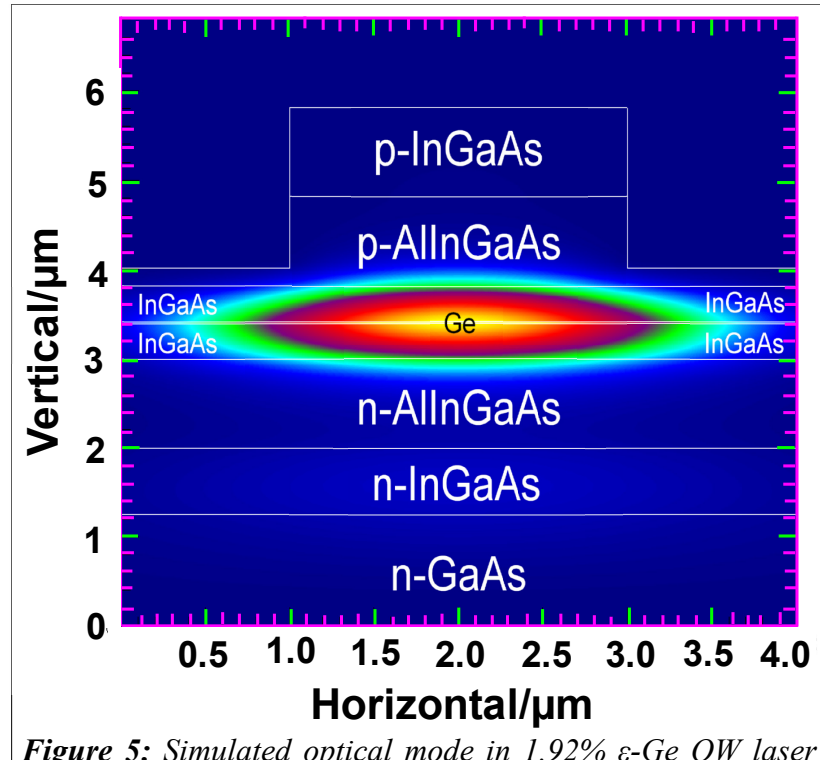


Figure 5: Simulated optical mode in 1.92% ε-Ge QW laser structure, shown in Figure 4, using FIMMWAVE.

and the Al_{0.3}In_{0.28}Ga_{0.42}As barrier layer prevent the optical mode penetration onto the bottom and upper InGaAs layer, supported by the simulated optical mode, shown in **Figure 5**. The ternary InGaAs layer on both side of the ε-Ge layer is for the ease of the growth of Ge QW laser structure during MBE growth process than direct growth of quaternary Al_{0.3}In_{0.28}Ga_{0.42}As layer on the top of ε-Ge layer. The bottom Al_{0.3}In_{0.28}Ga_{0.42}As layer growth is trivial than upper Al_{0.3}In_{0.28}Ga_{0.42}As layer due to the competition of add atom mobility of each constituent on the surface at growth temperature. Note that aluminium (Al) add atom mobility on growth surface is lower than either In or Ga,⁴³ thus needs higher growth temperature than In or Ga containing film. Therefore, the combination of Al_{0.3}In_{0.28}Ga_{0.42}As/In_{0.28}Ga_{0.72}As barrier layer on ε-Ge laser structure is indispensable for the consideration of growth as well as both carrier and optical confinement.

Laser efficiency is in large part determined by the dynamics of the carriers in the Ge lasing layer. Using a first-principles 30-band k.p electronic structure theory approach, $^{25, 40, 44}$ we have determined the optical gain, threshold current density J_{th} and loss mechanisms that dominate the laser structure. The direct band-to-band gain (G) was calculated using the full band structure of Ge at three strain configurations (0.2%, 1.62%, and 1.96%) including quantum confinement are shown in **Figure 6** at different injected carrier concentrations in the range from $3x10^{18}$ cm⁻³ to $9x10^{19}$ cm⁻³. The gain, G is calculated using, G

$$G = \frac{v}{\epsilon_0 n_b ch v_{\gamma}} \sum_{k,n,n'} \left| P_{k,n,n'} \right|^2 (f_{k,n}^c - f_{k,n'}^v - 1) \operatorname{sech} \left(\omega_{k,n,n'} - \nu \right), \tag{1}$$

where ν is the laser frequency, V is the active region volume, n_b is the background refractive index, γ is the dephasing rate (see Ref. 1), ϵ_0 and c are the permittivity and the speed of light in vacuum, and $\left|P_{k,n,n'}\right|^2$ is the dipole matrix for optical transition between crystal momentum k-points in the n conduction Γ - valley and n' heavy hole (HH)/light hole (LH) valleys, respectively. Finally, the contribution to the current density (J_{sp}) from spontaneous emission was calculated using, ¹

$$J_{sp} = ed \int_0^\infty d\nu \left(\frac{n_b \nu}{\pi c}\right)^2 G(\nu) \left[exp\left(\frac{\hbar \nu - \mu_{\rm eh}}{k_B T}\right) - 1\right]^{-1}, \tag{2}$$

where, d is the active region thickness, μ_{eh} is the electron-hole quasi-chemical potential energy separation that satisfies the transparency condition in the gain spectrum ($G(\nu) = 0$ at a given carrier concentration), and k_B is Boltzmann constant, respectively. To our knowledge, these are the first results that consider the entire electronic band structure for the calculation of gain in this material. We observe that higher strain increases the gain at higher wavelengths and lower injection concentrations. Note that the lowest injected carrier density is different for each figure due to the gain starting at different injections for the different strain induced band structures. The injected carrier density (N_I) for each strain level is indicated in Figure 6. In addition, the decreasing Ge thickness, required by higher strain due to critical layer thickness to avoid strain relaxation, can remove some of the advantages (i.e., gain) achieved by the strain. In order to address this, we have calculated the gain for 1.96% strained Ge at thicknesses of 15 nm and 30 nm, respectively, shown in Figures 6c and 6d. We found that the 1.62% or 1.96% strained Ge with 30 nm Ge layer thickness are among the best for gain as a function of photon energy, with gain also starting at lower injection carrier density. A Ge layer thickness of at least 30 nm and a strain level of >1.6% are needed for achieving higher gain at lower N_I . The tradeoff is between the achievable strained Ge thickness with highest tensile strain inside the Ge during growth, and the Ge layer thickness that must be reduced with higher strain to prevent strain relaxation in the tensile-strained Ge QW laser structure. Figure 7 shows the calculated maximum G obtained in the simulations shown in Figure 6 versus the current density (J_{sp}) : (a) where losses in the current are ignored and (b) includes an estimate of the losses due to Shockley-Read-Hall and Auger recombination processes based on data from Ref. [1]. To date, no reliable models of the free carrier absorption exist for this strained Ge material. We find that increasing strain from 0.2% to 1.62% can dramatically reduce J_{th} from 300 A/cm² to < 10 A/cm², respectively. If we disregard losses, increasing the strain further to 1.96% reduces the threshold current density even further, shown in **Figure 7b**. This gain in effectiveness is reduced to that of 1.62% if we include losses. This reduction in effectiveness is a direct consequence of the limit to the Ge QW thickness with higher strain inside the Ge layer. The

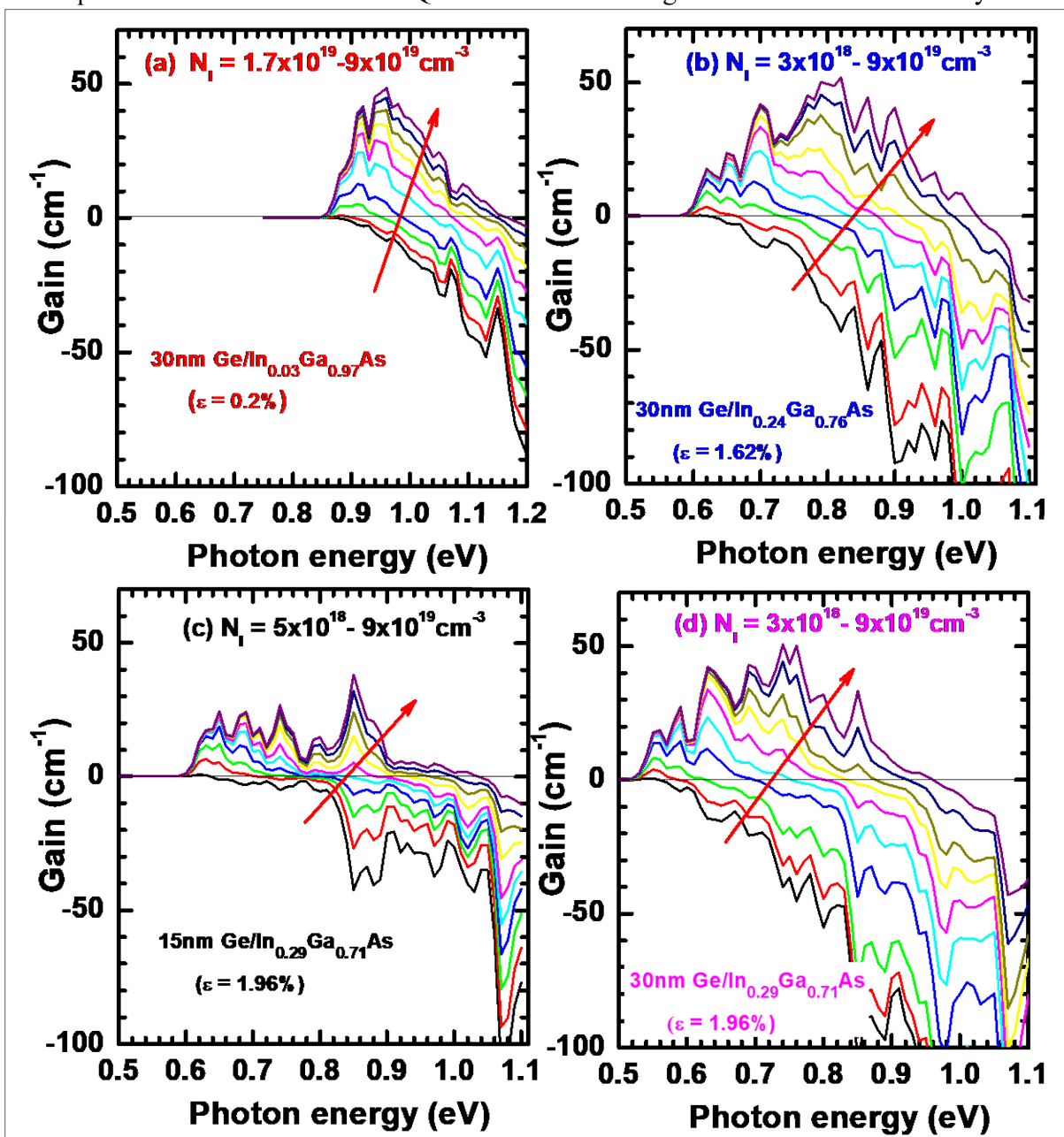


Figure 6: Calculated optical gain vs photon energy at 300K at various injected carrier densities N_I for (a) 30 nm Ge/ $In_{0.03}$ Ga_{0.97}As, strain $\varepsilon = 0.2\%$, (b) 30 nm Ge/ $In_{0.24}$ Ga_{0.76}As, with $\varepsilon = 1.62\%$, (c) 15 nm Ge/ $In_{0.29}$ Ga_{0.71}As with $\varepsilon = 1.96\%$ strain, and (d) 30 nm Ge/ $In_{0.29}$ Ga_{0.71}As with $\varepsilon = 1.96\%$ strain. The injected carrier density, N_I for each strain level in indicated in each figure. Here, higher strain increases the gain at higher wavelengths and lower injection concentrations, and > 1.6% strained with at least 30 nm Ge are needed for achieving higher gain at lower injection level.

thinner QW results in a smaller density of states and quantization effect, which limits the gain (see the difference in effective masses due to curvature change by strain in Fig. 1). On the other hand, if a 1.96% strain is achieved at thicknesses \geq 20 nm, the gain/threshold current ratio would be much superior than the same thickness and less strain, thanks to the higher direct band gap nature of Ge at higher strain. Therefore, one can find from the first principles calculation that the gain increases with lower energy for 1.96% strained Ge with increasing Ge thickness from 15 nm to 30nm and the threshold current density decreases with increasing strain and thickness, studied here. Thus, one needs to account for a feedback from experiments to realize a realistic model of the emission in this laser material.

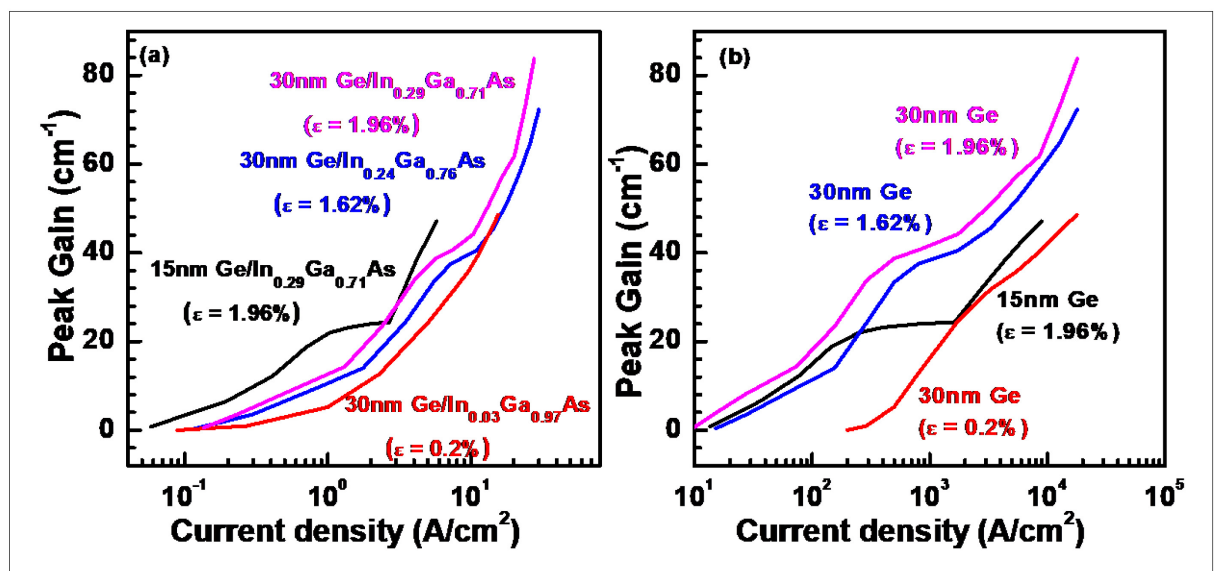


Figure 7: Calculated Peak Gain vs current density for three strain configurations. The current density is calculated (a) without and (b) with losses arising from non-radiative recombination.

Materials Analysis of ε -Ge and ε -Ge Laser Structure:

Defect analysis of ε-Ge epilayers via plan-view TEM: As we have showcased in Figure 7, the need for direct bandgap Ge for light sources *via* strain engineering, we have experimentally demonstrated the tunable tensile strained epitaxial ε-Ge layers in the strain ranges from 0.0% to $1.95\%^{31,35,38-40}$ on GaAs and Si substrates using InGaAs strain template as well as 1.6% and 1.95% strained InGaAs/ε-Ge/InGaAs QW structures on linearly graded In_xGa_{1-x}As

metamorphic buffer using solid source MBE. These structures were characterized using different analytical tools ^{31, 35, 38-40} to access the materials quality. In this aspect, the defect analysis using plan-view transmission electron microscopy (PV-TEM) is indispensable since the defects can cause the losses in the ε-Ge lasing media, as shown in **Figure 7b**. Thus, determination of the defect density is of utmost importance for mismatch epitaxy especially tensile strained Ge layer. **Figure 8a-b** shows the 0.7% ε-Ge and 1.2% ε-Ge layer structures grown on GaAs substrates using graded In_xGa_{1-x}As strain template and PV-TEM micrographs of each structure. It is worth noting that the MBE grown ε-Ge epilayer thicknesses, 15 nm (ε-Ge/In_{0.11}Ga_{0.89}As) and 30 nm (ε-Ge/In_{0.17}Ga_{0.83}As), remain well below the calculated critical layer thickness values, as we have recently reported³⁵ using People and Bean's energy balance model.⁴⁵ Therefore, it is expected that the strain relaxation in the epitaxial ε-Ge would be minimal which can cause an additional defects and dislocations. The dark band in each figure

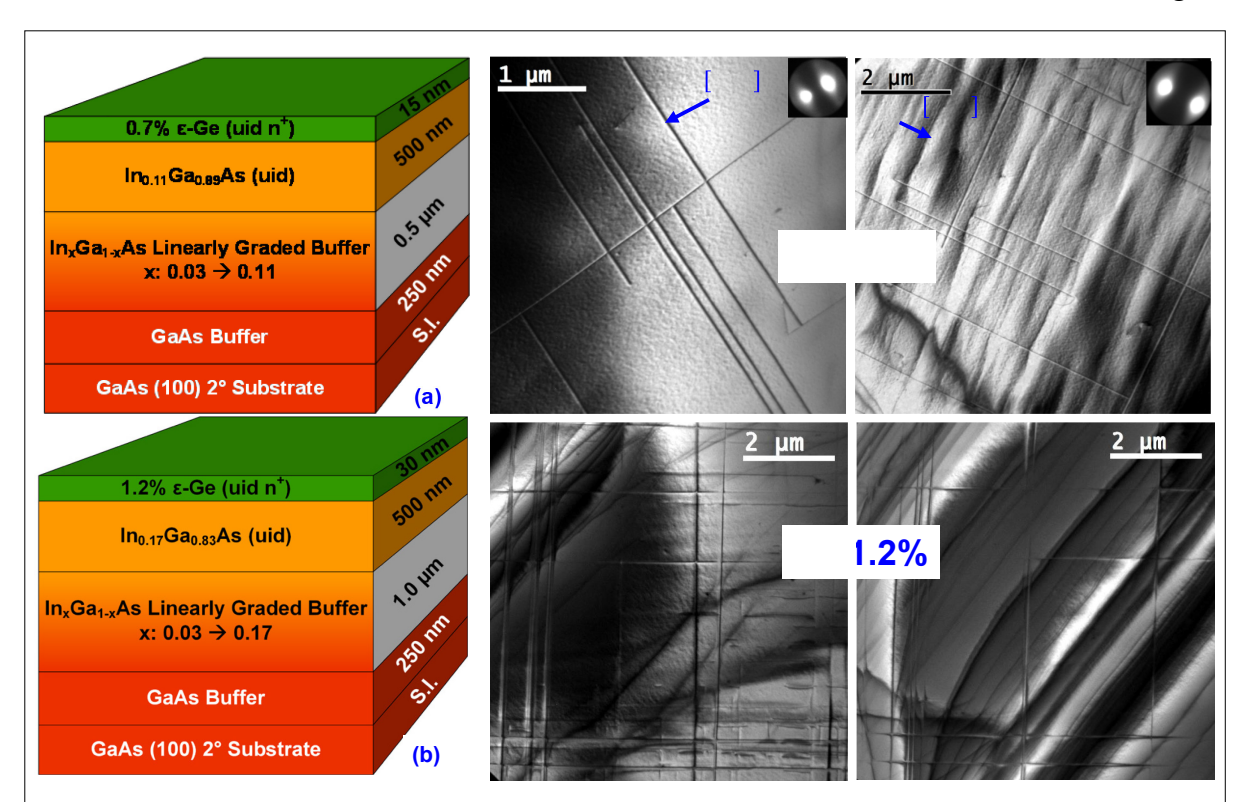


Figure 8: PV-TEM micrographs of (a) 0.7% ε -Ge and (b) 1.2% ε -Ge along with their materials growth structure, respectively. The misfit dislocation (MD) networks due to strain relaxation of buffer for each strain amount are clearly visible, implies superior growth of metamorphic buffer layer and tensile strained Ge on top of each strain amount.

is the bend contour, which is due to the lattice moving into and out of different Bragg diffraction conditions. The two dimensional misfit dislocation (MD) networks were clearly visible from each structure and are running in the two <110> orthogonal direction. Depending on their Burger vectors orientation of these MDs (i.e., parallel, antiparallel, perpendicular, etc), different types of interactions were possible. 46 In one such interaction, where Burger vectors are perpendicular, no L-reaction (i.e., no α and β dislocations cross-slip) is anticipated. One can find from Fig. 8a-b, the different misfit dislocation densities and its character of the dislocation network. Upon inspecting this figure, we found that the 1.2% ε-Ge sample showed an array of dislocations similar to 0.7% ε -Ge but with much longer dislocation segments that were closely spaced. As we know, the local strain fields of MDs are expected to occasionally react when orthogonal MDs intersect. These strain field reactions can cause MDs to repel each other resulting in L-reactions (both MDs change their glide direction by 90°). 47 L-reactions are statistically expected to occur at 16-25% of MD intersections in diamond and zinc blende materials when all dislocations have the usual $\mathbf{b} = \frac{1}{2} < 110 >$ type Burgers vectors. Here, we counted no Lreactions both 1.2% ε-Ge and 0.7% ε-Ge tensile strained Ge/InGaAs material system. We will explain the absence of L-reactions in this tensile system. The MDs in diamond or zinc blende materials glide in {111} slip planes and have Burgers vectors of the type $\mathbf{b} = \frac{1}{2} < 110 > \text{ usually}$ angled 60° from the dislocation line. Normally, such dislocations can easily cross-slip from one {111} plane to another. However, these MDs can also disassociate into Shockley partial dislocation (SPD) pairs with Burgers vectors of the type $\mathbf{b} = 1/6 < 112 >$. Furthermore, although it has not yet been shown in the Ge/InGaAs material system, however, MD disassociation has been shown to occur in tensile (100) oriented films in other material systems. 48-52 This is due to the fact that in (100) tensile system, the leading Shockley partial dislocation of a SPD pair, the 90° partial is pure edge component and has its Burgers vector completely aligned with the resolved shear stress on the $\{111\}$ planes, *i.e.* the misfit stress acts on the 90° partial very efficiently. Other configurations where this occurs are compressive (110) and (111) growth. ⁴⁹ Due to the alignment of the leading SPD Burgers vector and the resolved shear stress, MDs nucleate easier in these configurations, resulting in a downward shift in the critical layer thickness compared to compressive (100) growth. 52, 53 If the MDs near the surface were disassociated it would help explain their straightness since a SPD unlikely to exhibit cross-slip. We will explain the contrast of two orthogonal MDs below. Therefore, absence of L-reactions in the dislocation networks in 1.2% ε-Ge and 0.7% ε-Ge system is attributed to these networks being primarily disassociated 60° dislocations. This also implies the superior growth of relaxed metamorphic graded InGaAs buffer layer in each case, and subsequently the tensile-strained Ge layer growth on top of each graded buffer. This PV-TEM micrographs also allows us to determine the defect density of $\sim 1.2 \times 10^7$ cm⁻² and $< 4 \times 10^6$ cm⁻² for 0.7% and 1.2% strain, respectively. These TDD values are likely an upper bound, since it can also include TDDs from within the InGaAs virtual substrate, which complicates the accurate assignment of the dislocation density number solely within the ε -Ge layer. However, we have performed the defects analysis by the invisibility criterion $g \cdot b = 0$, where dislocation arrays (lines) that exhibit a loss of contrast (the disappearance of the leading partials, discussed below) are most-probably associated with defects formed in the ε-Ge epilayers. Therefore, some TDDs or MDs are most-probably exist within the ε -Ge epilayer. The individual MDs that form in the ε -Ge epilayer would likely not have sufficient time or energy to glide, and therefore form the neat MD arrays that we see in the PV-TEM images, if the epilayer remains mostly strained, as is the case here.

Invisibility criterion for disassociated misfit dislocations under plan-view TEM imaging: Complete Burgers vector analysis by the invisibility criterion $g \cdot b = 0$ was difficult. This is largely due to the inability to maintain a constant g vector over a sufficiently large region in a bent specimen foil. Moving to thicker regions where bending was minimized was not effective since these extremely thick regions give substantial dynamical diffraction contrast due to the

diffracted beam being re-diffracted multiple times, weakening the two-beam condition during measurement. However, in a moderately thick region (~ 400 nm) a constant low index <220> type g vector could be obtained over a small area, a few μ m², as shown in Figure 8a. Working within these limitations, we observed that MD lines parallel to the g vector at the ε -Ge/InGaAs interface retain significant residual contrast. This is shown in Figure 8a-b, and is also examined quantitatively in **Figure 9**, which is a magnification of the image given in Figure 8a. Dislocations lines in the 0.7% ε -Ge sample parallel to a <220> type g vector provided ~40% less contrast than lines perpendicular to g, as measured in Figure 9. As previously discussed, the MDs are expected to be disassociated in perfect 60° dislocations, with the separation distance between the SPDs being constrained by the 15 nm height of the ε -Ge film. A 60° dislocation with its line directed along the [$\overline{1}$ 01] direction, as shown in Figure 8a, with Burgers vector $\mathbf{b} = \frac{1}{2}[\overline{1}$ 01] will disassociate into a leading 90° SPD with $\mathbf{b} = \frac{1}{6}[\overline{1}\overline{1}$ 2] and a trailing 30°

partial with $\mathbf{b} = \frac{1}{6}[\overline{2}11]$. If \mathbf{g} is set to $[2\overline{2}0]$ as in Figure 8a, the leading pure-edge dislocation should vanish since both $\mathbf{g} \cdot \mathbf{b}$ and $\mathbf{g} \cdot (\mathbf{b} \times \mathbf{u})$ are both equal to zero, where \mathbf{u} is a unit vector parallel to the dislocation line. However, the trailing 30° partial will not lose contrast since $\mathbf{g} \cdot \mathbf{b} = -1$. At the scale of the image in Figure 8a, the contrast caused by the leading and trailing dislocations are virtually overlapping due to the narrow separation of the partials. Therefore, when the leading partial loses contrast due to the diffraction condition

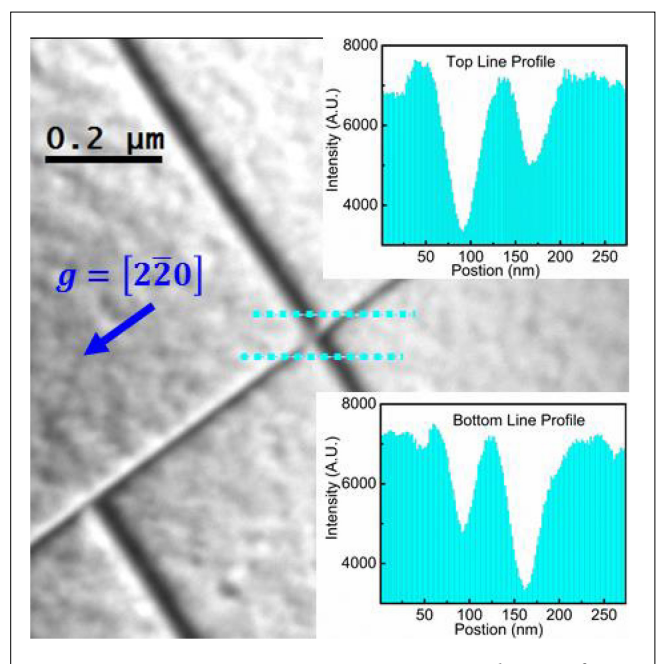


Figure 9: Quantitative contrast analysis of two orthogonal MDs. The dotted blue lines represent histogram line profiles of the intensity from the dislocation intersection shown in the top right of Figure 8a. The dislocation parallel to **g** has measurably reduced contrast.

we should still see a dislocation line due to the trailing partial, but the total contrast should be measurably reduced. This behavior is exactly what we have observed here. The loss of contrast appears to occur primarily on one side of the dislocation line, reflecting the non-zero separation distance between the leading (invisible) and trailing (visible) partials. Upon analyzing the detailed formation of MDs and their interactions, we can conclude that the defect density is in the well-controlled range of mismatch epitaxy ⁴⁶ and the room temperature photoluminescence properties is another important benchmarking property for tensile strained Ge, as discussed below.

Room-temperature photoluminescence properties of direct-bandgap 1.6% & Ge: An important design parameter considered for ε -Ge-based laser structure is the optical cladding material surrounding the direct bandgap Ge. The cladding material should provide both carrier and optical confinement in the ε -Ge layer, with minimal-to-negligible absorption. This cladding material should also permit light emission from the lasing media, ε -Ge $^{31, 35, 38-40}$ through the thinner upper barrier. The thickness and composition are also important such that

the refractive indices of the various layers are suitable for strong optical confinement as well as emission of laser wavelength due to the modification of bandgap via strain engineering in Ge. Figure 10 shows the observed room temperature photoluminescence (PL) intensities near the direct gap obtained from 30 nm thick

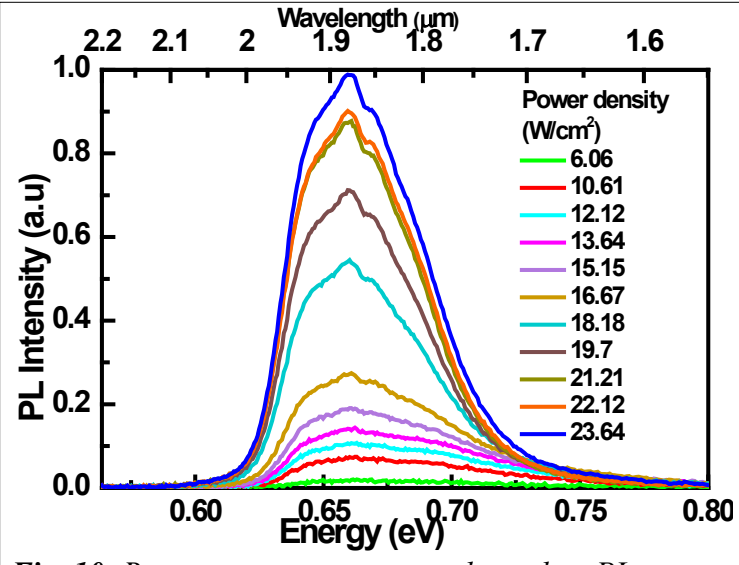


Fig. 10: Room temperature power dependent PL spectra of 1.6% tensile strained Ge layer on $In_{0.24}Ga_{0.76}As/In_xGa_{1-x}As/GaAs$, exhibiting the direct bandgap recombination.

1.6% ε-Ge layer grown GaAs substrate using graded In_xGa_{1-x}As metamorphic buffer as a function of excitation power varied from 6 W/cm² to 23 W/cm² under 700 nm Ti:Sa pulsed excitation mode. The spectra where obtained using InAs liquid nitrogen chilled detector. One can find from this figure that with increasing laser power, the peak luminescence intensity is increasing but the peak position remains at the same position. The lower energy side of each PL spectrum is slightly steeper than the high energy side. The direct bandgap luminescence line shape is less influenced by reabsorption due to the limited 30 nm thickness of Ge layer.⁵⁴ In addition, one can find from Figure 10 that the peak energy is at ~ 0.6609 eV, which is the direct bandgap transition from the conduction band at the Γ -valley to the heavy-hole (HH) transition or/and from the L-valley to HH transition. From Figure 1b, one can find that the energy levels of Γ - and L-valleys are almost at the same level, and the L-valley will still remain majority of excited electrons. For the minimum excitation power density of 6.06 W/cm², it is likely that minimal recombination was detectable due to insufficient filling of Γ -valley states as compared to the majorly-filled L-valley states. At higher excitation power density at this 1.6% strain level or at higher tensile strain states (e.g., 1.96%), strain-induced splitting of the Γ - and L-valley conduction band (CB) minima results in a lower significantly lower Γ -valley CB minimum, hence the direct bandgap optical transition from the Ge is possible. The peak energy position for this 1.6% tensile strained Ge at 300 K is in agreement with the bandgap versus misfit strain relation reported by Guiloy et al.⁵⁵ and Suess et al.⁵⁶ for Ge micro bridges by photo-reflectance spectroscopy at room temperature. It also agrees with the calculated optical gain versus photon energy shown in Figure 6b. In most of the literatures, ^{30, 31, 40, 44} the PL spectra were recorded from tensile strained Ge grown on III-V buffers at low temperature measurement and this result is the first room temperature PL spectra obtained from the 1.6% bi-axially strained Ge grown on InGaAs buffer. Moreover, this Ge/In_{0.24}Ga_{0.76}As sample revealed strong Fabry-Perot (FP) oscillations at the maximum of the gain curve. One can find

that the emission wavelength is centered at about 1.9 µm (Figure 10) and has wavelength span within full width at half maximum of ~150 nm. Once the strain amount inside the Ge is above 1.5%, the L-valley and Γ -valley are at the same conduction band minimum (see Fig. 1b), and hence the material is direct bandgap, as reported by our earlier work ^{31, 35, 38-40} and by others. ^{27,} 55, 56 Beyond the tensile strained amount of 1.5%, the optical transition must be from the conduction band at the Γ -valley to LH or HH. There is also evident the optical transition from the Γ-valley to LH. 40 Since the density of states are small in LH band compared with HH band due to lower effective mass when separated by strain, one can expect the optical transition from the conduction band at Γ -valley to the HH despite the fact the LH band is above the HH band, as shown in Figure 1. The carriers generated during higher optical excitation at the Γ -valley would not transferred to L-valley due to the steeper curvature of the Γ -valley than in L-valley. The Γ -valley states will be deeply populated as more carriers are injected by optical pumping. $^{21, 24, 57-59}$ It has been reported that the percentage of carrier population in Γ -valley increased with increasing optical excitation power.⁵⁹ One might assume that the indirect-to-direct crossover point might vary depending on the amount of tensile strain in Ge and indeed, several literatures reported the indirect-to-direct cross-over point in the range of 1.5-2% tensile strained

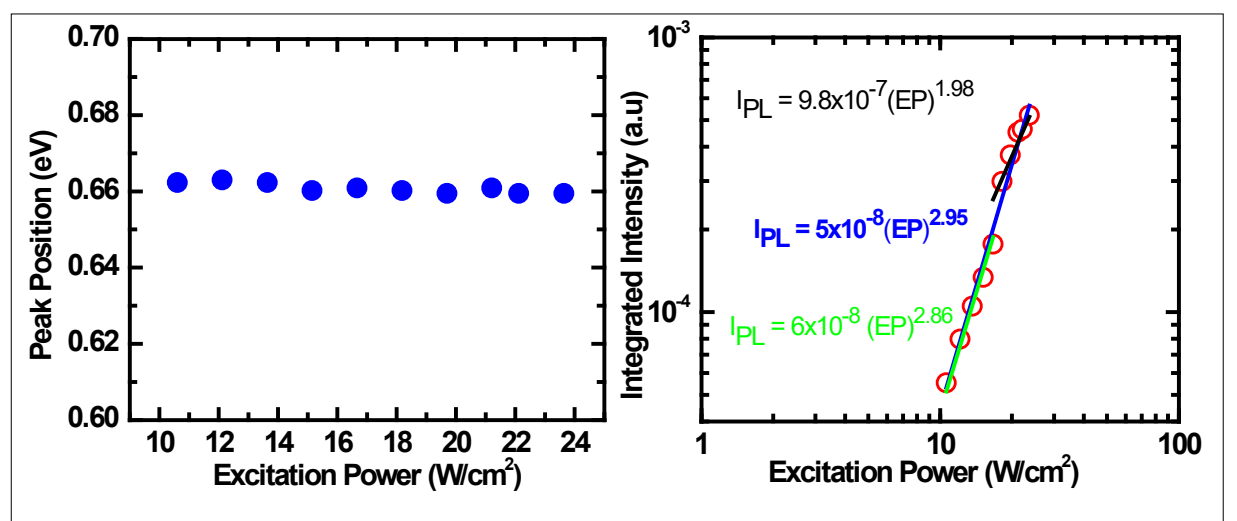


Fig. 11: (a) Peak position as a function of excitation power and (b) integrated peak intensity with excitation power.

in Ge.^{40, 55, 56} This makes an ambiguity whether the optical transition is indeed solely from the conduction band at the Γ - valley not from the L- valley. In order to confirm the optical transition, we have plotted the peak energy as well as integrated PL intensity as a function of excitation power. **Figure 11a** shows the peak energy obtained from Figure 10 as a function of excitation power density. One can find that the peak position remains constant with laser excitation power studied in this work, which is in agreement with the room temperature steady state recombination modelling results ⁵⁹ for biaxial tensile strained Ge with various strain levels from 0% to 2.5%. This further confirms the direct bandgap of Ge and the optical transition is from the Γ - valley due to the higher radiative recombination rate.

It has been widely reported that the laser power dependence on the near band edge PL can provide the nature of optical transition in semiconductors and their heterostructures. ^{27, 60-62} **Figure 11b** shows the integrated PL intensity (I_{PL}) obtained from Figure 10 as a function of excitation power. One can find that the luminescence intensity increases with excitation power. The I_{PL} is related to the excitation intensity through the relation, $I_{PL} = CP^k$, where C is a constant, P is the excitation power density, and k is the power factor. 61 It has been reported that the k < 2 is for indirect transition (e.g., L-to-HH) and k = 2 for the direct transition (Γ -to-HH) for Ge, since the PL intensity is proportional to the number of electrons and holes taking place during recombination process. From Figure 11b, one can find that the integrated luminescence intensity varies super linearly with excitation power, which is in agreement with the reported results by Jain et al., ⁵⁹ Klingenstein and Schweizer ⁵⁴ and by Arguirov et al. ⁶² for strained and unstrained Ge, respectively. The k values were obtained in the range of 1.98 to 2.95 depending on the data set used during fitting process. The extracted k value is 2 or well above 2. The power factor of k = 2.4 was reported by Jain et al. ⁵⁹ for 0.82% bi-axially tensile strained Ge using steady-state recombination modeling and k = 6.4 of experimentally. Therefore, we can conclude that the PL spectra obtained here are from the direct transition in the conduction band

at Γ -valley, and due to higher excitation, the direct recombination will occurs significantly than

non-radiative the recombination via defects or dislocations. Figure 12 is a zoom-in emission spectrum measured with high gain InGaAs detector, which is sensitive below 1.7 µm. One can find from this figure, the visible Fabry-Perot oscillation on the top of PL spectrum. This

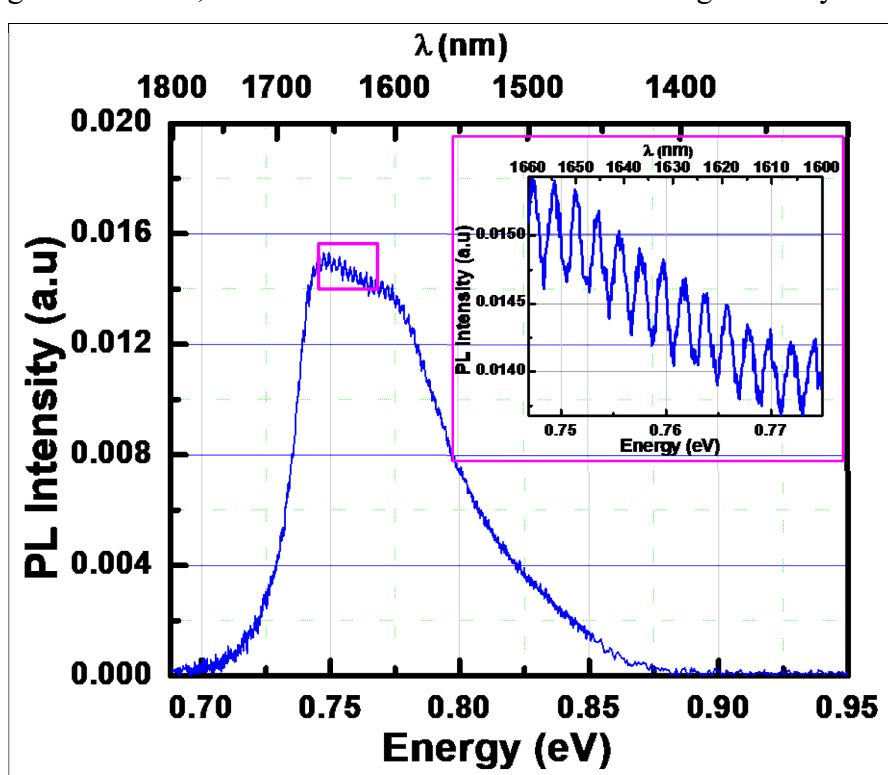


Fig. 12: Room temperature PL spectrum of 1.6% tensile strained Ge layer on $In_{0.24}Ga_{0.76}As/In_xGa_{1-x}As/GaAs$ measured using high gain InGaAs detector, displaying Fabry-Perot oscillation. Inset shows the zoom-in spectrum from the FP oscillation section.

signifies the quality of strained Ge material synthesis via MBE and its Ge/InGaAs heterointerface.

Strain analysis of ε -Ge/In_xGa_{1-x}As QW heterostructure via X-ray diffraction: Utilizing the design by FIMMWAVE mode solver of ε -Ge QW laser structure, as shown in Figure 2, we have grown the ε -Ge QW laser structure on GaAs substrate using interconnected dual chamber solid source MBE system. To determine the structural quality and relaxation state of Ge QW laser structure, reciprocal space maps (RSMs) of symmetric (004) and asymmetric (115), were recorded during x-ray measurement from this structure. Figure 13a-b shows (004) symmetric and (115) asymmetric RSMs, respectively, for this structure. Using the measured perpendicular and parallel lattice constants, we have determined the In composition in constant composition upper InGaAs layer. We have found that the targeted 13 nm ε -Ge QW layer is tensile strained

with respect to constant composition of In_{0.28}Ga_{0.72}As confinement layer that has provided ~ 1.95% amount of tensile-strained to Ge QW layer. In this laser structure, 2.0 μm upper In_{0.28}Ga_{0.72}As barrier layer (same thickness as bottom In_{0.28}Ga_{0.72}As barrier layer) was selected for carrier and optical confinement in ε-Ge QW. In the In_xGa_{1-x}As linearly graded buffer, we have selected an In overshoot composition of ~ 30% (~100 nm thickness) in order to fully relax the buffer layer when grown on GaAs substrate. The reciprocal lattice point (RLP) of Ge, In_{0.28}Ga_{0.72}As, graded InGaAs, and GaAs substrate are clearly visible in **Figure 13a-b**. One can find from (004) RSM that the ε-Ge layer is indeed tensile strained since the RLP of ε-Ge is located on the top RLP of GaAs substrate, and the small contour below the RLP of In_{0.28}Ga_{0.72}As layer is the RSM of overshoot In_{0.30}Ga_{0.70}As layer (the small hump below label In_{0.28}Ga_{0.72}As). The lowered growth temperature of 450°C compared to the bottom InGaAs layer growth temperature (525°C), was selected for the upper In_{0.28}Ga_{0.72}As layer growth on the top of 13 nm ε-Ge QW layer, just to make sure that the strain inside the 13 nm ε-Ge QW layer would not relax during the growth of upper 2 μm In_{0.28}Ga_{0.72}As layer. Whether the upper

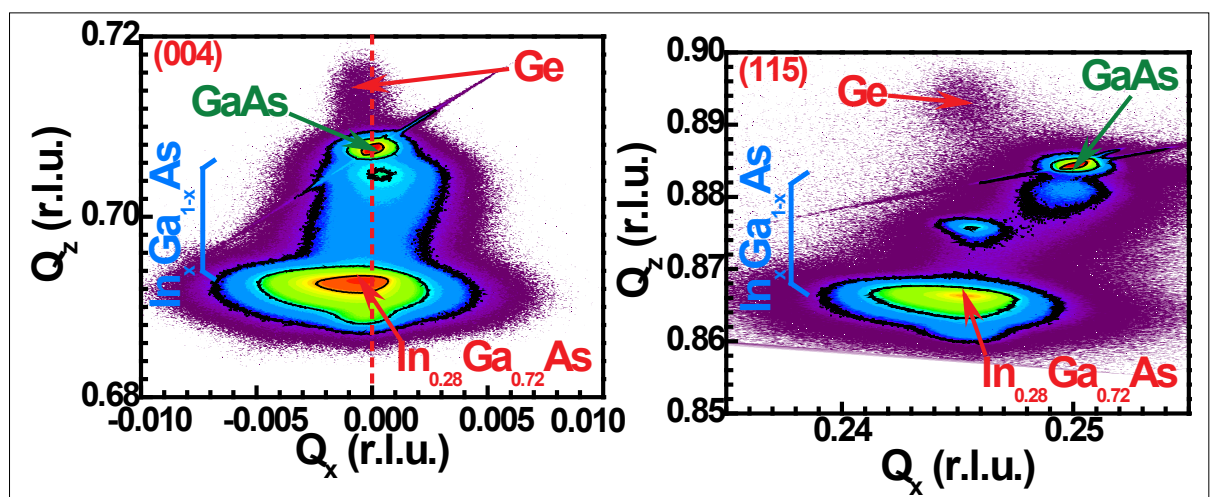


Figure 13: X-ray reciprocal space maps of (a) (004) symmetric and (b) (115) asymmetric scan from the $In_{0.28}Ga_{0.72}As/\varepsilon$ -Ge/ $In_{0.28}Ga_{0.72}As$ QW laser structure on GaAs substrate, respectively. All these results demonstrated the strained ε -Ge QW. The Ge is almost fully strained as indicated by the strained line shown in (a) as well as peak location of the Ge with respect to the GaAs substrate. Also, the RLP of Ge lies on the top of the RLP of constant composition $In_{0.28}Ga_{0.72}As$ layer, confirming the ε -Ge.

In_xGa_{1-x}As layer is relaxed or lattice matched with in-plane lattice constant of ε-Ge QW, crosssectional TEM microscopic analysis is essential. If the composition of the upper In_xGa_{1-x}As layer is different during growth on top of ε-Ge, one should expect RLP of that InGaAs layer beside the RLP of constant composition bottom In_{0.28}Ga_{0.72}As layer. Since there was no visible separate RLP of constant composition InGaAs layer from bottom and top layer, we can ensure that the upper In composition in InGaAs layer is almost identical as the bottom constant In composition of InGaAs. However, the broadness of the InGaAs contour is due to lattice constant distortions, i.e., defects induced broadening. By examining the cross-sectional TEM analysis of the structure, discussed below, we can infer that the lattice distortion broadening is due to the upper InGaAs layer. To further verify on this point, the thickness of the upper InGaAs epilayer is large (2.0 µm) compared to the overshoot layer within the metamorphic buffer (less than 100 nm). Accordingly, it should have a larger Bragg diffraction intensity. Due to this, it is possible that a portion of the lattice contour intensity between the primary InGaAs centroid (labeled, Figure 13a) and the overshoot layer centroid (the small, green "hump" in Figure 13a) is due to the upper InGaAs layer if the upper InGaAs layer were to have a larger lattice constant than the lower InGaAs layer. Explicitly, this would indicate that the upper InGaAs layer has a higher In composition than the lower InGaAs layer and thus, the lattice mismatch-induced defect formation in the upper InGaAs layer. This claim could be further supported by the absence of an additional diffraction centroid at higher Qz (lower lattice constant, lower In composition) than the main InGaAs centroid (labeled, Figure 13a). By considering the HR-XRD and cross-sectional TEM data together, we believe that the measured In composition more accurately reflects that of the lower InGaAs layer, whereas the upper InGaAs layer likely has a higher lattice constant (In composition), and was therefore found to be defective due to the lattice mismatch (evident in the cross-sectional TEM images below). Because of the defect-associated distortion to the upper InGaAs diffraction contour, and its relatively high intensity, the upper InGaAs diffraction contour exists as a "smear" between the labeled, lower InGaAs centroid and the unlabeled overshoot layer centroid. Thus, the referred RLP of In_{0.28}Ga_{0.72}As layer, as shown in Figure 13a-b, is the signal from both bottom and top In_xGa_{1-x}As layers. Therefore, RSMs of our 1.95% ϵ -Ge QW laser structure on GaAs with top In_xGa_{1-x}As (0.28<x<0.30) and bottom In_{0.28}Ga_{0.72}As barrier layers, demonstrated the quasi-pseudomorphic nature of the ϵ -Ge layer, where the ϵ -Ge lattice constant is in agreement with the in-plane lattice constant of the In_{0.28}Ga_{0.72}As bottom barrier layer.

Defect Analysis of ε-Ge/InxGa1-xAs QW Heterostructures via Cross-Sectional TEM: In addition to the x-ray analysis above, cross-sectional TEM analysis of ε-Ge QW laser structure is indispensable. The cross-sectional TEM micrographs of our 1.95% ε-Ge QW laser structure on GaAs with InGaAs barrier layers, are shown in **Figure 14**. The low- and high-magnification TEM micrographs, shown in **Figure 14a** and **14b**, corresponding to the entire ε-Ge laser structure and the ε-Ge/In_{0.28}Ga_{0.72}As heterointerface, respectively, highlighting the confinement of lattice mismatch-induced defects below the region of interest. As can be seen from Figure 14a, the linearly graded In_xGa_{1-x}As buffer accommodated the misfit strain via the

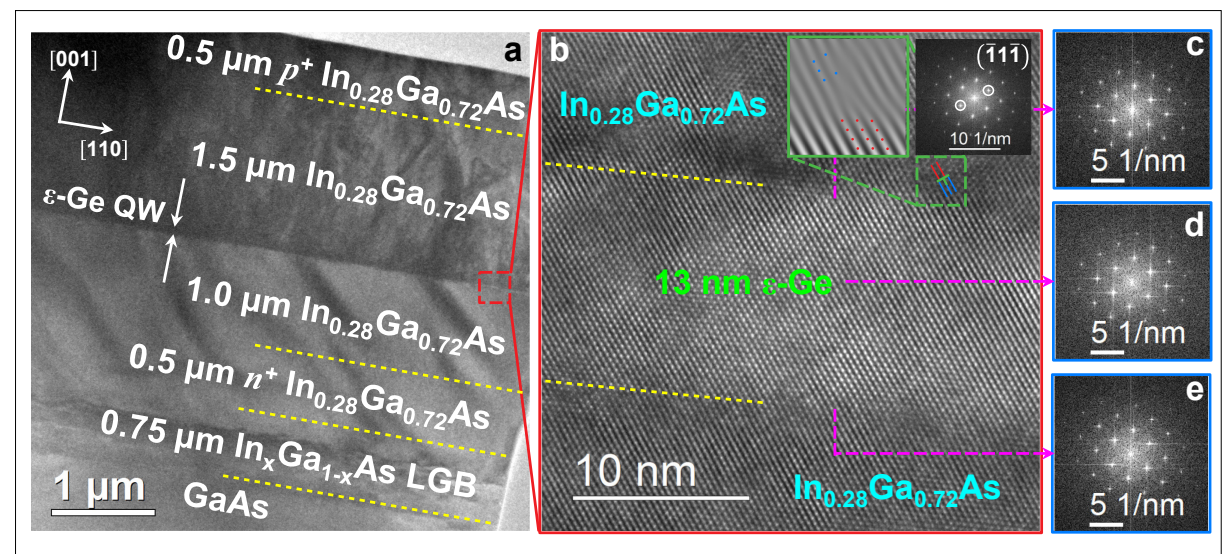


Figure 14: (a) Cross-sectional TEM of the entire laser structure, (b) HR-TEM view of the $In_{0.28}Ga_{0.72}As/\epsilon$ -Ge/ $In_{0.28}Ga_{0.72}As$ QW part, (c)-(e) FFT patterns from the upper $In_{0.28}Ga_{0.72}As/\epsilon$ -Ge, ϵ -Ge, ϵ -Ge/ $In_{0.28}Ga_{0.72}A$ heterointerface region, respectively. All these results demonstrated the strained ϵ -Ge QW.

formation and subsequent glide of threading dislocations, thereby preventing substantial defect propagation along the growth direction. Correspondingly, the constant-composition In_{0.28}Ga_{0.72}As stressor was observed to be absent of long-range microstructural defects or disorder, implicitly supporting the high degree of relaxation and crystallinity found *via* x-ray analysis above. Examining **Figure 14b**, one can find that the epitaxial ε-Ge and the constant composition In_{0.28}Ga_{0.72}As stressor exhibited a highly uniform heterointerface. Atom probe tomography study demonstrated 6Å heterointerface abruptness of Ge/In_{0.24}Ga_{0.76}As heterostructure (not shown here). The lattice indexing shows the lattice line extending from the ε-Ge layer to the In_{0.28}Ga_{0.72}As layer and it also shows that the Ge in-plane lattice constant internally matches with the lattice constant of In_{0.28}Ga_{0.72}As bottom layer, demonstrating the tensile strain ε-Ge, which is also supported by the x-ray analysis above (Fig. 13).

As we have demonstrated the tensile strained Ge on bottom In_{0.28}Ga_{0.72}As layer, the Fast-Fourier Transform (FFT) patterns were taken from the top In_{0.28}Ga_{0.72}As/ε-Ge heterointerface,

ε-Ge and ε -Ge/In_{0.28}Ga_{0.72}As heterointerface and the results were shown in Figures 14c, d, and e, respectively. These results suggest an atomically abrupt heterointerface of lacking visible atomic interdiffusion or relaxation-inducing misfit dislocations (MDs). The absence satellite reflections in Figures 13c-e confirms a single lattice constant (i.e., $a_{In0.28Ga0.72As} =$ a_{Ge}) to the diffractogram, thereby providing additional support for a quasi-

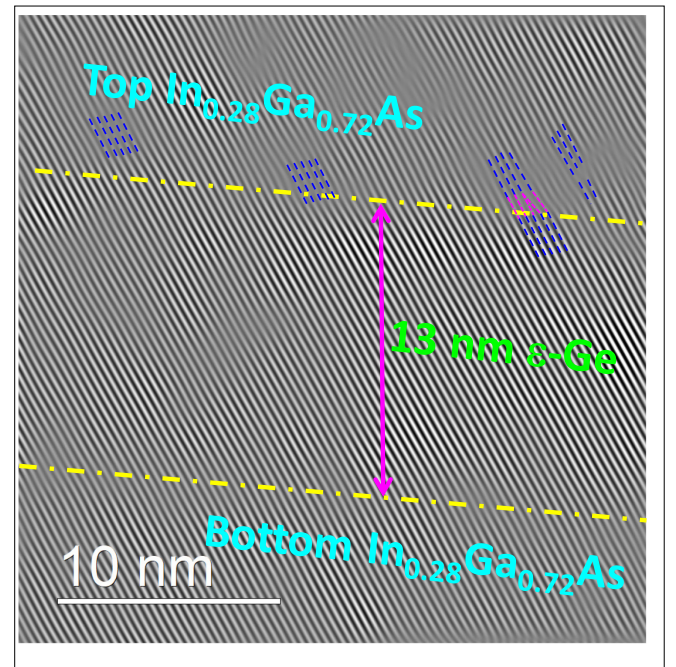


Figure 15: Filtered FFT pattern of the $In_{0.28}Ga_{0.72}As/\varepsilon$ -Ge/ $In_{0.28}Ga_{0.72}As$ QW laser structure, showing the misfit dislocations only in the upper $In_{0.28}Ga_{0.72}As$ layer.

ideal pseudomorphic Ge epitaxy, where the ε -Ge lattice constant matches with the in-plane lattice constant of the In_{0.28}Ga_{0.72}As bottom and upper barrier layers. In addition, the inverse FFT patterns were taken from both the top In_{0.28}Ga_{0.72}As/ε-Ge heterointerface and the In_{0.28}Ga_{0.72}As/ε-Ge/ In_{0.28}Ga_{0.72}As QW part to identify if there is any MDs present in the top or bottom heterointerface. The reconstructed HR-TEM micrograph from the top In_{0.28}Ga_{0.72}As/ε-Ge heterointerface shown in Figure 14b is used to identify the lattice lines at the interface, and hence to identify the types of dislocations present at the heterointerface. Figure 15 shows the inverse FFT pattern taken from the part of the In_{0.28}Ga_{0.72}As/ε-Ge/ In_{0.28}Ga_{0.72}As QW which shows the formation of MDs at the top InGaAs/ε-Ge heterointerface. One can find that the MDs only appeared in the upper In_{0.28}Ga_{0.72}As layer as a linear defects and are considered as an insertion of an extra half-plane of atoms (see blue-pink region) and none were present at the bottom heterointerface. This would suggest that there is some degree of lattice mismatch at this interface that resulted in defect formation and strain relaxation. The fact that these MDs are absent at the bottom ε-Ge/InGaAs heterointerface suggests that, on the other hand, the bottom heterointerface is perfectly lattice matched. Moreover, the thick 2 µm In_{0.28}Ga_{0.72}As upper barrier layer minimizes the relaxation of the entire ε -Ge lasing media of 13 nm, which is needed for a fixed wavelength light emission.

CONCLUSIONS

We have demonstrated the strain and bandgap engineered epitaxial ε -Ge layers as well as ε -Ge quantum-well laser structures through theoretical calculations and experimentally. The biaxial tensile strained in the range of 0.7% to 1.96% in ε -Ge layer were provided by the InGaAs stressor during materials synthesis using molecular beam epitaxy for optical and carrier confinement. The simulated direct band-to-band gain, threshold current density and loss mechanisms that dominate the ε -Ge QW laser structure were calculated. It has been shown that the higher strain increases the gain at higher wavelengths and at lower injection concentrations;

however, the decreasing ε-Ge QW thicknesses are needed for higher strains to avoid strain relaxation. In addition, the J_{th} can be greatly reduced from 300 A/cm² at 0.2% strain to <10 A/cm² at 1.96% strain level. The room temperature PL measurement demonstrated direct bandgap optical emission from the conduction band at Γ- valley to HH (0.6609 eV) from the 1.6% strained Ge/In_{0.24}Ga_{0.76}As heterostructure. The threading dislocation density is below 4×10^6 cm² for 1.2% ε-Ge, which is an upper bound, exhibited superior material quality. X-ray and transmission electron microscopy analysis of experimentally realistic 1.95% bi-axially strained In_{0.28}Ga_{0.72}As/13 nm ε-Ge/In_{0.28}Ga_{0.72}As QW laser structure demonstrated coherent epitaxy of ε-Ge on In_{0.28}Ga_{0.72}As barrier layers and minimal relaxation of the Ge layer. Therefore, our strain and bandgap engineered ε-Ge on GaAs and ultimately transfer the process to Si substrate using III-V metamorphic buffer, would provide a major step towards the integration of Ge-based photonic devices on Si.

MATERIALS AND METHODS

Electronic Structure Calculation. The calculations of the gain G and current density J are dependent on states of the whole Brillouin zone: the optical transitions occur around to the direct gap at Γ , while the density of states, carrier density and chemical potential have a larger dependence on the conduction band near the L valley. The electronic band structure across the whole Brillouin zone was calculated using the 30-band k.p approach of Ref. [63, 64]. The quantization condition was calculated using the "Truncated Crystal Approximation" ⁶⁵ by considering the k-points in each valley that are compatible with the boundary conditions given by the thickness of the QW assuming hard wall boundaries. We justify the use of hard wall boundaries, rather than a more exact softer approach such as that of Ref. [66], by the strong type I nature of the offset between the Ge and InGaAs layer, with Γ and L respective band offsets of 0.5 and close to 1 eV. This approximation allows us to calculate the quantized subbands across the whole Brillouin zone with the parameters of the Ge layer only, without the

need for iterations including the InGaAs layer. The detailed methodology of the electronic structure calculations was discussed under results and discussion. All parameters of the strained Ge band structure can be found in Ref. [63].

Material Synthesis. The epitaxial strained Ge layers in the thickness ranges from 13 nm to 75 nm and Ge quantum-well laser structure was grown on semi-insulating (100)/2° GaAs substrates. Vacuum interconnected solid source molecular beam epitaxy growth chambers one for Ge and another for III-V materials, were used for materials synthesis. The growth temperature and growth rate of epitaxial Ge were 400°C and 0.1 Å/s, respectively. In brief, the GaAs oxide desorption was taken at 750°C, measured by thermocouple, under arsenic over pressure of $\sim 10^{-5}$ torr. After the oxide desorption, the 250 nm thick undoped GaAs was grown at 650°C prior to the linearly graded In_xGa_{1-x}As metamorphic buffer layer to a targeted In composition of 0.28 for 1.95% strained Ge QW structure. Within the 0.75 µm thick In_xGa_{1-x}As linearly graded buffer, 100 nm thick In_{0.30}Ga_{0.70}As layer was inserted in order for the faster relaxation of the InGaAs graded buffer layer for acting as virtual substrate. The bottom barrier In_{0.28}Ga_{0.72}As layer thickness of 1.5 μm was grown prior to the 13 nm Ge layer growth on top of this constant composition In_{0.28}Ga_{0.72}As layer, which act as a bottom barrier layer. Note that sample was vacuum transferred to Ge MBE chamber for Ge layer growth and then back to III-V MBE chamber for upper 2.0 µm thick InGaAs layer growth. The growth temperature of bottom and upper InGaAs layer were 525°C and 450°C, and the growth rate was fixed at 0.7 μm/hr, respectively. The details of the growth procedure are reported elsewhere. ^{31, 35, 38} Materials Characterization. High-resolution x-ray diffraction measurements using Panalytical MRD Pro with PIXcel and triple axis detection capability were recorded for determination of the structural quality and the relaxation state of epitaxial Ge layers. Cross-sectional and planview transmission electron microscopy analysis were performed to determine the entire laser

structure and defect density within the strained Ge layers. The HR-TEM imaging was

performed using TITAN transmission electron microscope and image processing were

performed using Gatan image filtering software. For this purpose, the electron transparent foil

of thin film cross-section and plan-view of the selective strained Ge and laser structure were

prepared by a standard polishing technique. The PV-TEM imaging was performed using JEOL

2100 transmission electron microscope. Room temperature photoluminescence measurements

were performed to determine the bandgap of tensile strained Ge using a Ti:Sa pulsed laser as a

source of excitation with a variable excitation intensity, as indicated on Figure 8. Both liquid

nitrogen cooled InGaAs and InAs detectors were used to collect the signal from the sample.

The detailed of the measurement setup and procedure of collecting data from sample surface

were recently reported.⁴⁰

AUTHOR INFORMATION

Corresponding Author

*Tel: (540) 231-6663. Fax: (540) 231-3362. E-mail: mantu.hudait@vt.edu.

ORCID

Mantu K. Hudait: <u>0000-0002-9789-3081</u>

Michael B. Clavel: 0000-0002-2925-6099

Shuvodip Bhattacharya: 0000-0002-3778-3307

Notes

The authors declare no competing financial interest.

ACKNOWLEDGEMENTS

M.B.C. and M. K. H. acknowledges partial support from the NSF under grant number ECCS-

1507950 and ECCS-2042079, a US-Ireland joint R&D program. Authors acknowledge NCFL-

Institute for Critical Technology and Applied Science and Virginia Tech Nanofabrication

facilities for materials characterization. The authors also acknowledge Dr. Luke F. Lester for

31

several insightful technical discussions related to this work. FMA acknowledges Science Foundation Ireland grants SFI/14/US/I3057, 17/QERA/3473 and 19/FFP/6953.

Additional information

Correspondence and requests for materials should be addressed to M. H.

REFERENCES

- (1) Chow, W. W. Model for direct-transition gain in a Ge-on-Si laser. *Appl. Phys. Lett.* **2012**, *100*, 191113.
- (2) Elbaz, A.; Buca, D.; von den Driesch, N.; Pantzas, K.; Patriarche, G.; Zerounian, N.; Herth, E.; Checoury, X.; Sauvage, S.; Sagnes, I.; Foti, A.; Ossikovski, R.; Hartmann, J. M.; Boeuf, F.; Ikonic, Z.; Boucaud, P.; Grützmacher, D.; El Kurdi, M. Ultra-low-threshold continuous-wave and pulsed lasing in tensile-strained GeSn alloys. *Nat. Photonics* 2020, 14, 375-382.
- (3) Soref, R. A.; Buca, D.; Yu, S. -Q. Group IV photonics-driving integrated optoelectronics. *Opt. Photon. News* **2016**, *27*, 32-39.
- (4) Stange, D.; Wirths, S.; Geiger, R.; Schulte-Braucks, C.; Marzban, B.; von den Driesch, N.; Mussler, G.; Zabel, T.; Stoica, T.; Hartmann, J. -M.; Mantl, S.; Ikonic, Z.; Grützmacher, D.; Sigg, H.; Witzens, J.; Buca, D. Optically Pumped GeSn Microdisk Lasers on Si. ACS Photonics 2016, 3, 1279-1285.
- (5) Al-Kabi, S.; Amir Ghetmiri, S. d.; Margetis, J.; Pham, T.; Zhou, Y.; Dou, W.; Collier, B.; Quinde, R.; Du, W.; Mosleh, A.; Liu, J.; Sun, G.; Soref, R. A.; Tolle, J.; Li, B.; Mortazavi, M.; Naseem, H. A.; Yu, S. -Q. An optically pumped 2.5 μm GeSn laser on Si operating at 110 K. Appl. Phy. Lett. 2016 109, 171105.
- (6) Singh, V.; Lin, P. T.; Patel, N.; Lin, H.; Li, L.; Zou, Y.; Deng, F.; Ni, C.; Hu, J.; Giammarco, J.; Paola Soliani, A.; Zdyrko, B.; Luzinov, I.; Novak, S.; Novak, J.; Wachtel, P.; Danto, S.; Musgraves, J. D.; Richardson, K.; Kimerling, L. C.; Agarwal, A. M. Midinfrared materials and devices on a Si platform for optical sensing. *Sci. Technol. Adv. Mater.* 2014, 15, 2-14.
- (7) Zhou, Y.; Dou, W.; Du, W.; Ojo, S.; Tran, H.; Ghetmiri, S. A.; Liu, J.; Sun, G.; Soref, R.; Margetis, J.; Tolle, J.; Li, B.; Chen, Z.; Mortazavi, M.; Yu, S. –Q. Optically Pumped

- GeSn Lasers Operating at 270 K with Broad Waveguide Structures on Si. *ACS Photonics* **2019**, *6*, 1434-1441.
- (8) Bao, S.; Kim, D.; Onwukaeme, C.; Gupta, S.; Saraswat, K.; Lee, K. H.; Kim, Y.; Min, D.; Jung, Y.; Qiu, H.; Wang, H.; Fitzgerald, E. A.; Tan, C. S.; Nam, D. Low-threshold optically pumped lasing in highly strained germanium nanowires. *Nat Commun.* 2017, 8, 1845.
- (9) von den Driesch, N.; Stange, D.; Wirths, S.; Mussler, G.; Holländer, B.; Ikonic, Z.; Hartmann, J. M.; Stoica, T.; Mantl, S.; Grützmacher, D.; Buca, D. Direct Bandgap Group IV Epitaxy on Si for Laser Applications. *Chem. Mater.* **2015**, *27*, 4693-4702.
- (10) Wang, Z.; Abbasi, A.; Dave, U.; De Groote, A.; Kumari, S.; Kunert, B.; Merckling, C.; Pantouvaki, M.; Shi, Y.; Tian, B.; Van Gasse, K.; Verbist, J.; Wang, R.; Xie, W.; Zhang, J.; Zhu, Y.; Bauwelinck, J.; Yin, X.; Hens, Z.; Van Campenhout, J.; Kuyken, B.; Baets, R.; Morthier, G.; Van Thourhout, D.; Roelkens, G. Novel Light Source Integration Approaches for Silicon Photonics. *Laser Photonics Rev.* 2017, 11, 1700063.
- (11) Seifried, M.; Villares, G.; Baumgartner, Y.; Hahn, H.; Halter, M.; Horst, F.; Caimi, D.; Caer, C.; Sousa, M.; Dangel, R. F.; Czornomaz, L.; Offrein, B. J. Monolithically Integrated CMOS-Compatible III–V on Silicon Lasers. *IEEE J. Sel. Top. Quantum Electron.* 2018, 24, 1-9.
- (12) Wang, H.; Kim, D.; Harfouche, M.; Santis, C. T.; Satyan, N.; Rakuljic, G.; Yariv, A. Narrow-Linewidth Oxide-Confined Heterogeneously Integrated Si/III–V Semiconductor Lasers. *IEEE Photon. Technol. Lett.* **2017**, *29*, 2199-2202.
- (13) Fadaly, E. M. T.; Dijkstra, A.; Suckert, J. R.; Ziss, D.; van Tilburg, M. A. J.; Mao, C.; Ren, Y.; van Lange; V. T.; Korzun, K.; Kölling, S.; Verheijen, M. A.; Busse, D.; Rödl, C.; Furthmüller, J.; Bechstedt, F.; Stangl, J.; Finley, J. J.; Botti, S.; Haverkort, J. E. M.;

- Bakkers, E. P. A. M. Direct-bandgap emission from hexagonal Ge and SiGe alloys. *Nature* **2020**, *580*, 205.
- (14) Nishizawa, N.; Kawagoe, H.; Yamanaka, M.; Matsushima, M.; Mori, K.; Kawabe, T. Wavelength Dependence of Ultrahigh-Resolution Optical Coherence Tomography Using Supercontinuum for Biomedical Imaging. *IEEE J. Sel. Top. Quantum Electron.* 2019, 25, 1-15.
- (15) Golovynskyi, S.; Golovynska, I.; Stepanova, L. I.; Datsenko, O. I.; Liu, L.; Qu, J.; Ohulchanskyy, T. Y. Optical windows for head tissues in near-infrared and short-wave infrared regions: Approaching transcranial light applications. *J. Biophotonics* 2018, 11, e201800141.
- (16) Zhu, B.; Kwon, S.; Rasmussen, J. C.; Litorja, M.; Sevick-Muraca, E. M. Comparison of NIR Versus SWIR Fluorescence Image Device Performance Using Working Standards Calibrated with SI Units. *IEEE Trans. Med. Imaging* 2020, 39, 944-951.
- (17) Wilson, R. H.; Nadeau, K. P.; Jaworski, F. B.; Tromberg, B. J.; Durkin, A. J. Review of short-wave infrared spectroscopy and imaging methods for biological tissue characterization. *J. Biomed. Opt.* **2015**, *20*, 030901.
- (18) Sun, C.; Wade, M. T.; Lee, Y.; Orcutt, J. S.; Alloatti, L.; Georgas, M. S.; Waterman, A. S.; Shainline, J. M.; Avizienis, R. R.; Lin, S.; Moss, B. R.; Kumar, R.; Pavanello, F.; Atabaki, A. H.; Cook, H. M.; Ou, A. J.; Leu, J. C.; Chen, Y. –H.; Asanović, K.; Ram, R. J.; Popović, M. A.; Stojanović, V. M. Single-chip microprocessor that communicates directly using light. *Nature* 2015, 528, 534.
- (19) Liang, D.; Bowers, J. E. Recent Progress in Lasers on Silicon. *Nat. Photonics* **2010**, *4*, 511-517.
- (20) Koshida, N.; Koyama, H. Visible Electroluminescence from Porous Silicon. *Appl. Phys. Lett.* **1992**, *60*, 347-349.

- (21) Cai, Y.; Han, Z.; Wang, X.; Camacho-Aguilera, R. E.; Kimerling, L. C.; Michel, J.; Liu, J. Analysis of Threshold Current Behavior forBulk and Quantum-Well Germanium Laser Structures. *IEEE J. Sel. Top. Quantum Electron.* 2013,19, 1901009.
- (22) Rong, H.; Liu, A.; Jones, R.; Cohen, O.; Hak, D.; Nicolaescu, R.; Fang, A.; Paniccia, M. An all-Silicon Raman Laser. *Nature* **2005**, *433*, 292-294.
- (23) Kuo, Y. H.; Lee, Y. K.; Ge, Y.; Ren. S.; Roth, J. E.; Kamins, T. I.; Miller, D. A. B.; Harris, J. S. Strong Quantum-Confined Stark Effect in Germanium Quantum-Well Structures on Silicon. *Nature* **2005**, *437*, 1334-1336.
- (24) Liu, J.; Sun, X.; Camacho-Aguilera, R.; Kimerling, L. C.; Michel, J. Ge-on-Si Laser Operating at Room Temperature. *Opt. Lett.* **2010**, *35*, 679-681.
- (25) El Kurdi, M.; Fishman, G.; Sauvage, S.; Boucaud, P. BandStructure and Optical Gain of Tensile-Strained Germanium Based on a 30 Band **k·p** Formalism. *J. Appl. Phys.* **2010**, *107*, 013710.
- (26) Duan, G. -H.; Jany, C.; Le Liepvre, A.; Accard, A.; Lamponi, M.; Make, D.; Kaspar, P.; Levaufre, G.; Girard, N.; Lelarge, F.; Fedeli, J. M.; Messaoudene, S.; Bordel, D.; Olivier, S. Hybrid III-V on Silicon Lasers for Photonic Integrated Circuits on Silicon. *Proc. SPIE* 2014, 9002, 90020X-1—90020X-6.
- (27) Wada, K.; Kimerling, L. C. *Photonics and Electronics with Germanium*. (1st Edition; Wiley-VCH Verlag GmbH & Co. KGaA, Boschst, 12, 69469 Weinheim, Germany, 2015).
- (28) Dutt, B. R.; Sukhdeo, D. S.; Nam, D.; Vulovic, B. M.; Yuan, Z.; Saraswat, K. C. Roadmap to an Efficient Germanium-on-Silicon Laser: Strain vs. n-type Doping. *IEEE J. Photonics* **2012**, *4*, 2002-2009.

- (29) Wirths, S.; Geiger, R.; von den Driesch, N.; Mussler, G.; Stoica, T.; Mantl, S.; Ikonic, Z.;
 Luysberg, M.; Chiussi, S.; Hartmann, J. M.; Sigg, H.; Faist, J.; Buca, D.; Grutzmacher,
 D. Lasing in Direct-Bandgap GeSn Alloy Grown on Si. *Nat. Photonics* 2015, *9*, 88-92.
- (30) Sanchez-Perez, J. R.; Boztug, C.; Chen, F.; Sudradjat, F. F.; Paskiewicz, D. M.; Jacobson, R. B.; Lagally, M. G.; Paiella, R. Direct-Bandgap Light-Emitting Germanium in Tensilely Strained Nanomembranes. *Proc. Natl. Acad. Sci. U. S. A.* 2011, 108, 18893-18898.
- (31) Clavel, M.; Saladukha, D.; Goley, P.; Ochalski, T. J.; Murphy-Armando, F.; Bodnar, R. J.; Hudait, M. K. Heterogeneously-Grown Tunable Tensile Strained Germanium on Silicon for Photonic Devices. ACS Appl. Mater. Inter. 2015, 7, 26470-26481.
- (32) Yang, J.; Bhattacharya, P.; Wu, Z.; Monolithic Integration of InGaAs-GaAs Quantum-Dot Laser and Quantum-Well Electroabsorption Modulator on Silicon. *IEEE Photon. Tech. Lett.* **2007**, *19*, 747-749.
- (33) Groenert, M. E.; Leitz, C. W.; Pitera, A. J.; Yang, V.; Lee, H.; Ram, R. J.; Fitzgerald, E. A. Monolithic Integration of Room-temperature GaAs/AlGaAs Lasers on Si Substrates via Relaxed Graded GeSi Buffer Layers. *J. Appl. Phys.* 2003, 93, 362-367.
- (34) Liu, J. F.; Sun, X.; Pan, D.; Wang, X. X.; Kimerling, L. C.; Koch, T. L.; Michel, J. Tensile-Strained, n-type Ge as a Gain Medium for Monolithic Laser Integration on Si. Opt. Express 2007, 15, 11272-11277.
- (35) Clavel, M.; Goley, P. S.; Jain, N.; Zhu, Y.; Hudait, M. K. Strain Engineered Biaxial Tensile Epitaxial Germanium for High-Performance Ge/InGaAs Tunnel Field-Effect Transistors. *IEEE J. Elec. Dev. Soc.* **2015**, *3*, 184-193.
- (36) FIMMWAVE/FIMMPROP by Photon Design Ltd., http://www.photond.com; March 2020.

- (37) Hudait, M. K.; Clavel, M.; Goley, P.; Jain, N.; Zhu, Y. Heterogeneous Integration of Epitaxial Ge on Si using AlAs/GaAs Buffer Architecture: Suitability for Low-power Fin Field-Effect Transistors. *Sci. Rep.* **2014**, *4*, 6964-6969.
- (38) Zhu, Y.; Maurya, D.; Priya, S.; Hudait, M. K. Tensile-Strained Nanoscale Ge/In_{0.16}Ga_{0.84}As Heterostructure for Tunnel Field-Effect Transistor. *ACS Appl. Mater. Inter.* **2014**, *6*, 4947-4953.
- (39) Hudait, M. K.; Clavel, M. B.; Lester, L.; Saladukha, D.; Ochalski, T. J.; Murphy-Armando, F. Heterogeneously grown tunable group-IV laser on silicon. *Proc. SPIE 9755, Quantum Sensing and Nano Electronics and Photonics XIII, 97550Y* (February 13, 2016).
- (40) Saladukha, D.; Clavel, M. B.; Murphy-Armando, F.; Greene-Diniz,G.; Gruening, M.; Hudait, M. K.; Ochalski. T. J. Direct and indirect band gaps in Ge under biaxial tensile strain investigated by photoluminescence and photoreflectance studies. *Phys. Rev.* B **2018**, *97*, 195304-1-12.
- (41) Hudait, M. K.; Clavel, M.; Goley, P.; Xie, Y.; Heremans, J. J. Magnetotransport Properties of Epitaxial Ge/AlAs Heterostructure Integrated on GaAs and Silicon. *ACS Appl. Mater. Inter.* **2015**, 7,22315-22321.
- (42) Greene-Diniz, G.; Grüning, M. First-Principles Calculations of Band Offsets at Heterovalent ε-Ge/In_xAl_{1-x}As Interfaces. *Phys. Rev. Appl.* **2018**, *10*, 044052.
- (43) Hudait, M. K.; Lin, Y.; Palmisiano, M. N.; Tivarus; C.; Pelz, J. P.; Ringel, S. A. Comparison of mixed anion, InAs_yP_{1-y} and mixed cation, In_xAl_{1-x}As metamorphic buffers grown by molecular beam epitaxy on (100) InP substrates. *J. Appl. Phys.* **2004**, *95*, 3952-3960.
- (44) Pavarelli, N.; Ochalski, T. J.; Murphy-Armando, F.; Huo, Y.; Schmidt, M.; Huyet, G.; Harris, J. S. Optical Emission of a Strained Direct-Band-Gap Ge Quantum Well Embedded Inside InGaAs Alloy Layers. *Phys. Rev. Lett.* 2013,110, 17740.

- (45) People, P.; Bean, J. C. Calculation of critical layer thickness versus lattice mismatch for Ge_xSi_{1-x}/Si strained-layer heterostructures. *Appl. Phys. Lett.* **1985**, *47*, 322-324.
- (46) Ayers, J. E.; Kujofsa, T.; Rago, P.; Raphael, J. E. *Heteroepitaxy of Semiconductors: Theory, Growth, and Characterization* (2nd edition, CRC Press, Boca Raton, FL, USA, 2017).
- (47) Dixon, R.; Goodhew, P. On the origin of misfit dislocations in InGaAs/GaAs strained layers. *J. Appl. Phys.* **1990**, *68*, 3163-3168.
- (48) Maree, P.; Barbour, J.; Van der Veen, J.; Kavanagh, K.; Bulle-Lieuwma, C.; Viegers, M., Generation of misfit dislocations in semiconductors. *J. Appl. Phys.* **1987**, *62*, 4413-4420.
- (49) Kvam, E.; Hull, R. Surface orientation and stacking fault generation in strained epitaxial growth. *J. Appl. Phys.* **1993**, *73*, 7407-7411.
- (50) Petruzzello, J.; Leys, M. Effect of the sign of misfit strain on the dislocation structure at interfaces of heteroepitaxial GaAs_xP_{1-x} films. *Appl. Phys. Lett.* **1988**, *53*, 2414-2416.
- (51) Hirashita, N.; Sugiyama, N.; Toyoda, E.; Takagi, S.-I. Relaxation processes in strained Si layers on silicon-germanium-on-insulator substrates. *Appl. Phys. Lett.* **2005**, *86*, 221923.
- (52) Hwang, D.; Bhat, R.; Schwarz, S.; Chen, C. In *Partial Dislocations and Critical Thicknesses for Strained Layer Relaxation*, MRS Proceedings, Cambridge Univ Press: 1992; p 421.
- (53) Hull, R.; Bean, J.; Peticolas, L.; Bahnck, D., Growth of Ge_xSi_{1-x} alloys on Si (110) surfaces. *Appl. Phys. Lett.* **1991**, *59*, 964-966.
- (54) Klingenstein, W.; Schweizer, H. Direct Gap Recombination in Germanium at High Excitation Level and Low Temperature. *Solid-State Electron.* **1978**, *21*, 1371-1374.
- (55) Guilloy, K.; Pauc, N.; Gassenq, A.; Niquet, Y. –M.; Escalante, J. –M.; Duchemin, I.; Tardif, S.; Dias, G. O.; Rouchon, D.; Widiez, J.; Hartmann, J. –M.; Geiger, R.; Zabel, T.; Sigg, H.; Faist, J.; Chelnokov, A.; Reboud, V.; Calvo, V. Germanium under High Tensile

- Stress: Nonlinear Dependence of Direct Band Gap vs Strain. ACS Photonics 2016, 3, 1907-1911.
- (56) Suess, M. J.; Geiger, R.; Minamisawa, R. A.; Schiefler, G.; Frigerio, J.; Chrastina, D.; Isella, G.; Spolenak, R.; Faist, J.; Sigg, H. Analysis of enhanced light emission from highly strained germanium microbridges. *Nat. Photonics* **2013**, *7*, 466-472.
- (57) Camacho-Aguilera, R. E.; Cai, Y.; Patel, N.; Bessette, J. T.; Romagnoli, M.; Kimerling, L. C.; Michel, J. An Electrically Pumped Germanium Laser. *Opt. Express* 2012, 20, 11316-11320.
- (58) Liu, J.; Sun, X.; Kimerling, L. C.; Michel, J. Direct-gap Optical Gain of Ge on Si at Room Temperature. *Opt. Lett.* **2009**, *34*, 1738–1740.
- (59) Jain, J. R.; Hryciw, A.; M. Baer, T.; Miller, D. A. B.; Brongersma, M. L.; Howe, R. T. A micromachining-based technology for enhancing germanium light emission via tensile strain", *Nat. Photonic* **2012**, *6*, 398-405.
- (60) Swaminathan, V.; Macrander, A. T. *Materials Aspects of GaAs and InP Based Structures*(Prentice Hall, Englewood Cliffs, New Jersey, 1991).
- (61) Schmidt, T.; Lischka, K. Excitation-power dependence of the near-band-edge photoluminescence of semiconductors. *Phys. Rev.* B, **1992**, *45*, 8989-8994.
- (62) Arguirov, T.; Kittler, M.; Abrosimov, N. V. Room temperature luminescence from Germanium. *J. Phys.: Conference Series* **2011**, *281*, 012021-8.
- (63) Rideau, D.; Feraille, M.; Ciampolini, L.; Minondo, M.; Tavernier, C.; Jaouen, H.; Ghetti, A. Strained Si, Ge, and Si_{1-x}Ge_x alloys modeled with a first-principles-optimized full-zone k·p method. *Phys. Rev.* B **2006**, *74*, 195208.
- (64) Hybertsen, M. S; Louie, S. G. Electron correlation in semiconductors and insulators: Band gaps and quasiparticle energies. *Phys. Rev.* B **1986**, *34*, 5390.

- (65) Zhang, S. B.; Yeh, C.-Y.; Zunger, A. Electronic structure of semiconductor quantum films. *Phys. Rev.* B, **1993**, *48*, 11204.
- (66) Richard, S.; Aniel, F.; Fishman G. Band diagrams of Si and Ge quantum wells via the 30-band k·p method. *Phys. Rev. B* **2005**, *72*, 245316-1-7.

TABLE OF CONTENTS FIGURE

